Icarus 313 (2018) 38–60

Contents lists available at ScienceDirect

Icarus

journal homepage: www.elsevier.com/locate/icarus

UV irradiation of biomarkers adsorbed on minerals under Martian-like conditions: Hints for life detection on Mars☆

Teresa Fornaro[a,b,*], Arjen Boosman[c], John R. Brucato[b], Inge Loes ten Kate[c], Sandra Siljeström[d], Giovanni Poggiali[b,e], Andrew Steele[a], Robert M. Hazen[a]

[a] Geophysical Laboratory of the Carnegie Institution for Science, Washington, DC, USA
[b] INAF-Astrophysical Observatory of Arcetri, Firenze, Italy
[c] Earth Sciences Department, Utrecht University, Utrecht, The Netherlands
[d] RISE Research Institutes of Sweden, Stockholm, Sweden
[e] Università degli Studi di Firenze, Dipartimento di Fisica ed Astronomia, Firenze, Italy

ARTICLE INFO

Article history:
Received 8 November 2017
Revised 24 April 2018
Accepted 1 May 2018
Available online 14 May 2018

Keywords:
Mars soil analogues
Biomarkers
Laboratory simulations
Infrared spectroscopy
Raman spectroscopy
ToF-SIMS

ABSTRACT

Laboratory simulations of Martian conditions are essential to develop quantitative models for the survival of organic biomarkers for future Mars exploration missions.

In this work, we report the results of ultraviolet (UV) irradiation processing of biomarkers adsorbed on minerals under Martian-like conditions. Specifically, we prepared Mars soil analogues by doping forsterite, lizardite, antigorite, labradorite, natrolite, apatite and hematite minerals with organic compounds considered as potential biomarkers of extant terrestrial life such as the nucleotides adenosine monophosphate (AMP) and uridine monophosphate (UMP). We characterized such Mars soil analogues by means of Time-of-Flight Secondary Ion Mass Spectrometry (ToF-SIMS), Diffuse Reflectance Infrared Fourier Transform Spectroscopy (DRIFTS) and Confocal Raman Imaging Spectroscopy (CRIS), in order to get insights into the specific molecule-mineral interactions and explore the capabilities of different techniques to reveal diagnostic features of these biomarkers. Then, we performed irradiation experiments in the mid-UV spectral region under simulated Martian conditions and under terrestrial ambient conditions for comparison, monitoring the degradation process through DRIFTS.

We observed that degradation under Martian-like conditions occurs much slower than in terrestrial ambient conditions. The minerals labradorite and natrolite mainly promote photodegradation of nucleotides, hematite and forsterite exhibit an intermediate degrading effect, while apatite, lizardite and antigorite do not show any significant catalytic effect on the degradation of the target organic species.

© 2018 Elsevier Inc. All rights reserved.

1. Introduction

Life detection within planetary exploration has always been an inspiring challenge that needs essential support from laboratory simulation studies. The possibility to simulate planetary environmental conditions gives key information about the processing that potential organic biomarkers might have experienced on other planets, and helps in the development of flight instruments and selection of landing sites focused on increasing the probability of detection of specific chemical compounds.

The planet Mars is a primary target of future life detection space missions. Indeed, the recent discovery of the preservation of small organic compounds at the harsh conditions on the surface of Mars, along with the presence of organics in Martian meteorites, is particularly encouraging for life detection (Freissinet et al., 2016, 2015; Glavin et al., 2013; Steele et al., 2016, 2012). The *Mars Science Laboratory* mission (*MSL*) has assessed the past habitabil-

☆ Electronic Supplementary Information (ESI) available: (i) powder X-Ray Diffraction (XRD) patterns for mineral samples; (ii) Infrared vibrational frequencies of nucleotides, both pure and adsorbed on different minerals, along with the vibrational shifts with respect to the pure nucleotides; (iii) Destruction cross-sections σ, formation cross-sections σ_f, and the half-lifetimes relative to the Martian UV flux $t_{1/2}{}_{\text{Mars}}$ obtained from *in situ* UV irradiation experiments in ambient terrestrial conditions for each detectable infrared peak of AMP and UMP, both pure and adsorbed at equilibrium on lizardite mineral; (iv) Percentages of degradation after 40 hours of UV irradiation of the equilibrium samples inside the PALLAS chamber for each detected infrared peak of the nucleotide; (v) Infrared spectra of nucleotides adsorbed on the different minerals before and after 40 hours UV irradiation under Martian-like conditions inside the PALLAS chamber.

* Corresponding author at: Geophysical Laboratory of the Carnegie Institution for Science, 5251 Broad Branch Rd. NW, Washington, DC 20015 USA.
E-mail address: tfornaro@carnegiescience.edu (T. Fornaro).

https://doi.org/10.1016/j.icarus.2018.05.001
0019-1035/© 2018 Elsevier Inc. All rights reserved.

ity of Mars by studying regolith and geological samples in Gale crater and verifying that ancient Mars harbored the geochemical complexity necessary to support microbial life (Grotzinger, 2014). During the Noachian era, about 4.1 to 3.7 billion years ago, Mars had a magnetic field, a thicker atmosphere, intense volcanic activity and higher temperatures compatible with the presence of liquid water on the surface. Early Mars should have received the same input of organic compounds as early Earth from the Late Heavy Bombardment (Gomes et al., 2005). Furthermore, there is ample evidence from Martian meteorites that Mars has been undertaking organic chemistry for most of its history (Steele et al., 2016, 2012). Thus, the emergence of more complex biochemistry from simple organic chemistry and chemical precursors under more Earth-like conditions is plausible. Then, Mars gradually lost its magnetic field and atmosphere, leading to lower temperatures that caused the formation of a thick cryosphere, where any water is frozen (Clifford et al., 2010). Mars' current geologic epoch, the so-called Amazonian, is characterized by less than 10 millibars atmosphere, which is predominantly (~ 96%) carbon dioxide (Mahaffy et al., 2013). Such a thin atmosphere produces a minimal greenhouse effect, leading to very low temperatures ranging from 145 K during the polar night to 300 K on the equator at midday at the closest point in Mars' orbit around the Sun, with diurnal variations of up to 80–100 K (Smith et al., 2004). The planet now appears arid and its recent mineralogy is characterized by the formation of anhydrous ferric oxides providing the typical red color of the surface. The thin atmosphere allows ionizing radiations such as energetic solar protons, galactic cosmic rays and ultraviolet (UV) photons to reach the surface of the planet (Cockell, 1998; Cockell et al., 2000; Hassler et al., 2014; Patel et al., 2003, 2002) and drive photochemical production of strong oxidants, such as perchlorates, in the soil (Georgiou et al., 2015; Glavin et al., 2013; Hunten, 1979; Kounaves et al., 2014; Yen et al., 2000). These are among the main factors that possibly drive degradation of organic compounds in the regolith on the surface of Mars (Benner et al., 2000; Biemann, 1979; Foustoukos and Stern, 2012; Klein et al., 1976; Ming et al., 2009; Quinn et al., 2013). However, without wide resurfacing processes, traces of putative ancient life-forms might be found in the oldest mineral deposits isolated within protected environments in the subsurface or recently made accessible at the surface due to erosion, faulting or impacts (Westall, 1999). Tentative detection of organics on the surface of Mars has recently occurred at the Gale crater, a site remnant of an ancient lake. Specifically, chlorinated hydrocarbons have been found through the *Sample Analysis at Mars* (*SAM*) instrument on board *MSL*'s *Curiosity* rover (Freissinet et al., 2015; Glavin et al., 2013). The provenance of these compounds is under continued debate, however, they may in part be derived from reactions taking place at high temperatures inside the *SAM* instrument between perchlorates/oxychlorine and complex aromatic and aliphatic precursor organic compounds indigenous to the sample (Freissinet et al., 2015; Miller et al., 2016). Additional sulfur-containing organics were discovered, that could have been either released as such from the sample or formed inside *SAM* by combination of sulfur from sulfur dioxide and organics released from the sample during high-temperature pyrolysis (Eigenbrode et al., 2016; Franz et al., 2017; Freissinet et al., 2016). It is not trivial to distinguish the nature of the organic precursors of the compounds formed inside the *SAM* instrument and their biotic or abiotic origin. Every year Mars receives an influx of abiotically-produced organics of 100 - 900 tons, by meteoritic, asteroidal, and cometary delivery (Crismani et al., 2017; Flynn, 1996; Frantseva et al., 2018), which may account for the presence of organics on the surface of the planet. Moreover, Mars meteorites have shown to possess an inventory of organic carbon formed through both igneous and secondary processes that may constitute the refractory pool of organics analyzed by SAM (Grady et al., 2004; McKay et al., 1996; Steele et al., 2016, 2012; Wright et al., 1992).

For a correct interpretation of the data collected on the ground during *in situ* exploration space missions such as *MSL*, it is key to understand how possible biotic and abiotic compounds are transformed due to the variety of phenomena that take place on the surface of Mars. Laboratory simulations of the harsh Martian conditions provide support to Mars exploration missions because they are indispensable to evaluate the likelihood of preservation of potential biomarkers on Mars and to develop technologies for detecting specific compounds (dos Santos et al., 2016; Fornaro et al., 2013a, 2013b, 2013c; ten Kate et al., 2006, 2005; ten Kate and Reuver, 2016). The thin carbon dioxide atmosphere of Mars is able to absorb far-UV radiations and X-rays but it lets other ionizing radiations penetrate, such as UV radiations with wavelength above 190 nm, gamma-rays, energetic solar protons and galactic cosmic rays, which may significantly affect organics in the regolith (Dartnell et al., 2007; Huestis et al., 2008; Jain et al., 2012; Patel et al., 2002). Specifically, the UV flux on the surface of Mars in the 190–325 nm spectral region, assuming a dust free atmosphere at the noontime equator, is of 1.4×10^{15} photons s^{-1} cm^{-2} (Patel et al., 2002). Even though UV radiation can penetrate only few microns or millimetres into the soil (Schuerger et al., 2012), it has been demonstrated that degradation of organic compounds by UV radiation occurs in timescales that are much shorter (*i.e.* days/months) than energetic particles or higher-energy radiation (*i.e.* hundreds of millions of years) capable of penetrating up to 2 m (Fornaro et al., 2013b; Gerakines and Hudson, 2013; Kminek and Bada, 2006; Poch et al., 2015, 2014). Therefore, irradiation in the mid-UV spectral range is among the main degradation agents on Mars that is worth simulating in order to inspect the stability and reactivity of possible biomarkers in the eolian-mobile layer and in the fresh subsurface materials exposed at the surface of Mars by impact gardening.

A huge effort is required to take into account all the combinatorial possibilities reflecting the wide geochemical complexity of the planet. Different mineral matrices may behave in a different manner in the presence of UV radiation by shielding molecules (Biondi et al., 2016, 2007; dos Santos et al., 2016; Ertem, 2004; Ertem et al., 2016; Franchi and Gallori, 2004; Gallori et al., 2004; Poch et al., 2015, 2014; Scappini et al., 2004) or promoting photolysis, photocatalysis and photosynthesis (Brucato et al., 2006; Emeline et al., 2003; Fornaro et al., 2013b; Garry et al., 2006; Saladino et al., 2015, 2013, 2011; Schoonen et al., 2004; Senanayake and Idriss, 2006; Shkrob et al., 2011). A systematic study of the effects of UV radiation on a variety of possible Mars soil analogues would be highly advantageous to elucidate which mineral deposits are more suitable to preservation of potential biomarkers on Mars, helping the selection of landing sites for future space missions.

In this work, we have investigated the catalytic/protective effects of different minerals relevant for Mars' mineralogy on important biomarkers of extant life. Specifically, we report the results of UV irradiation of Mars soil analogues prepared by doping labradorite, natrolite, forsterite, hematite, apatite, lizardite, and antigorite minerals, with the nucleic acid components adenosine monophosphate and uridine monophosphate. Irradiation was performed in the mid-UV spectral region because the UV flux on the surface of Mars is significant only in the 190–400 nm spectral range due to absorption and scattering by the Martian atmosphere at shorter wavelengths, as above-mentioned (Patel et al., 2002). Previous irradiation experiments of nucleic acid components in the mid-UV region (Fornaro et al., 2013b) confirmed that Xenon lamps provide a good simulation of irradiation processes occurring on such organic molecules in space and reliable evaluation of cross-sections. Indeed, the main photochemistry for heterocyclic aromatic compounds, such as nucleic acid components, per-

tains to the wavelenght range 200–300 nm where these molecules show the greatest absorption of photons and consequently the higher probability of degradation. Such experiments were carried out both under terrestrial ambient conditions and inside a Martian simulation chamber designed to mimic Martian-like atmospheric and temperature conditions (ten Kate and Reuver, 2016). Mars soil analogues were characterized by means of Time-of-Flight Secondary Ion Mass Spectrometry (ToF-SIMS), Diffuse Reflectance Infrared Fourier Transform Spectroscopy (DRIFTS) and Confocal Raman Imaging Spectroscopy (CRIS).

2. The relevance of the molecule-mineral systems under study

The purpose of this work was to investigate the photostability of adenosine monophosphate and uridine monophosphate, which are considered primary biomarkers of extant life because they are components of the informational biomolecules for terrestrial life, *i.e.* the nucleic acids DNA and RNA. Nucleic acids feature photoprotective properties thanks to the electronic structure of their chromophores, the nitrogenous bases. Indeed, upon electronic excitation, effective ultrafast photophysical decay can occur through conical intersection between the excited state and the ground state (Gustavsson et al., 2010, 2006, 2002a, 2002b, Santoro et al., 2010, 2009). This relaxation process makes excited states very short, reducing the probability of photochemical reactions. Such a photophysical behaviour might have been particularly advantageous to preserve nucleobases in high UV irradiation environments like Mars or early Earth.

In the planetary context, it is extremely interesting to study the changes of photostability of these molecules due to interactions with mineral matrices under plausible environmental conditions. We have compared the behaviour of minerals belonging to different classes that are abundant on Mars such as labradorite, natrolite, forsterite, hematite, apatite, lizardite and antigorite serpentine minerals, under irradiation in the mid-UV range in Martian-like atmosphere and temperature.

Specifically, we have considered lizardite and antigorite that are rock-forming hydroxylated magnesium iron polymorph phyllosilicates belonging to the serpentine subgroup with generic formula $(Mg,Fe)_3Si_2O_5(OH)_4$. Serpentines have been detected on Mars by the *Compact Reconnaissance Imaging Spectrometer for Mars* (*CRISM*) on the *Mars Reconnaissance Orbiter* (*MRO*) (Ehlmann et al., 2011, 2010, 2009; Viviano-Beck et al., 2014). On Earth these minerals form thanks to the serpentinization process, a hydration and metamorphic alteration of ultramafic rocks from Earth's mantle (Bach et al., 2006). During such a process, the oxidation of iron in olivine takes place, reducing water to produce molecular hydrogen, with subsequent production of methane, hydrocarbons and minerals like magnetite, brucite and serpentine (McCollom and Donaldson, 2016). It has been argued that serpentinization might be an abiotic source for methane on Mars (Atreya et al., 2007; Etiope et al., 2013; Oze and Sharma, 2005). Phyllosilicates are a primary class of minerals detected on Mars, and indicate that liquid water was present on the planet in the past because they derive from aqueous alteration of igneous rocks. Their formation goes back to the Noachian era, so they can be found in the oldest terrains currently buried by younger deposits or recently exposed in spots thanks to various phenomena such as weathering, erosion, or impact events (Bibring et al., 2006). These minerals draw great attention because they might host signatures of possible lifeforms developed during a flourishing past epoch in the history of Mars. Also, phyllosilicate minerals might have played key roles in prebiotic processes (Cairns-Smith and Hartman, 1986). Many studies point out that the high surface area and the structure of these minerals may be optimal for the adsorption of organic molecules. Indeed, phyllosilicates form parallel sheets of silicate tetrahedra with interlayer sites that are suitable for concentrating organic molecules on a local scale and providing protection against external environment (Biondi et al., 2007; Scappini et al., 2004).

Our study has focused also on other primary silicates detected on Mars from landed and orbital data sets (Ehlmann and Edwards, 2014), including the plagioclase feldspar labradorite with generic formula $(Ca, Na)(Al, Si)_4O_8$ and the zeolite natrolite, which is a hydrated sodium and aluminium tectosilicate with the formula $Na_2Al_2Si_3O_{10}{\cdot}2H_2O$.

Moreover, we have investigated a representative of mafic minerals, namely the magnesium-rich end-member of olivine, forsterite (Mg_2SiO_4), which is ubiquitous on terrestrial planets and moons (Chevrier and Mathé, 2007; Messenger et al., 2005; Poteet et al., 2011; Weinbruch et al., 2000). *OMEGA* and previous instruments have shown that pyroxene and olivine are still present at the surface of Mars in the older terrains, included within sand dunes, associated to early Noachian crustal rocks and early Hesperian volcanism (Bibring et al., 2006, 2005; Morrison et al., 2018; Ody et al., 2013).

Furthermore, we studied the iron oxide hematite (Fe_2O_3) that has been widely detected at Terra Meridiani, Aram Chaos near Valles Marineris, Aureum Chaos, Columbia Hills, Gale crater in younger layers uphill Mount Sharp (Arvidson et al., 2006; Bell et al., 2000; Catling and Moore, 2003; Christensen et al., 2001, 2000; Fraeman et al., 2013; Klingelhöfer et al., 2004; Souza-Egipsy et al., 2006). At Meridiani planum, the Opportunity rover detected a significant amount of hematite in the form of small spherules, apparently concretions precipitated by groundwater (Souza-Egipsy et al., 2006). Since formation of hematite may involve chemical precipitation from aqueous fluids under either ambient or hydrothermal conditions, this mineral is considered a "water-signature" iron oxide. The Curiosity rover is currently analyzing the composition of Mount Sharp at Gale crater, observing that hematite has replaced less-oxidized magnetite as the dominant iron oxide at higher, younger layers of Mount Sharp. The increase in hematite relative to magnetite suggests warmer, more oxidative conditions, or more interaction between sediments and atmosphere (Fraeman et al., 2013), because the formation of hematite may occur from precipitation upon exposure of anoxic Fe^{2+}-rich groundwater to an oxidizing environment, or from in-place weathering of precursor silicate materials under oxidizing conditions.

Finally, we studied the properties of the phosphate mineral apatite, which is a mixture of hydroxylapatite, fluorapatite and chlorapatite, and whose formula can be written as $Ca_{10}(PO_4)_6(OH,F,Cl)_2$. This mineral has been detected within several Martian meteorites such as ALH84001, Los Angeles, GRV 020090, Nakhla, and Shergotty (Greenwood et al., 2003; Hallis et al., 2012; Hu et al., 2014; McCubbin et al., 2014). Apatite is ubiquitous in extraterrestrial materials and it is a key mineral to look for distribution of volatiles including water in the Solar System because of its wide diversity in terms of chemical composition and very robust structure capable of retaining volatiles during thermal or shock events (McCubbin and Jones, 2015). Apatite is the only hydrous phase present in all Martian meteorites recognized so far, and it has been specifically used to quantify the presence of water in the Martian mantle (approximately 100 ppm) pointing out a close association between magmatic and hydrothermal activity on Mars (McCubbin and Jones, 2015 and references therein). Moreover, apatite is a source of phosphorus, an essential nutrient for terrestrial life, and therefore may be important in characterizing habitability on Mars (Hausrath et al., 2008; Hausrath and Tschauner, 2013; McCubbin and Jones, 2015; Palomba et al., 2004; Schwartz, 2006; Sun et al., 2014). Martian apatite has shown to be rich in chlorine (2.5–6.5 wt%) (McCubbin and Jones, 2015 and references therein), which determines higher solubility in aqueous

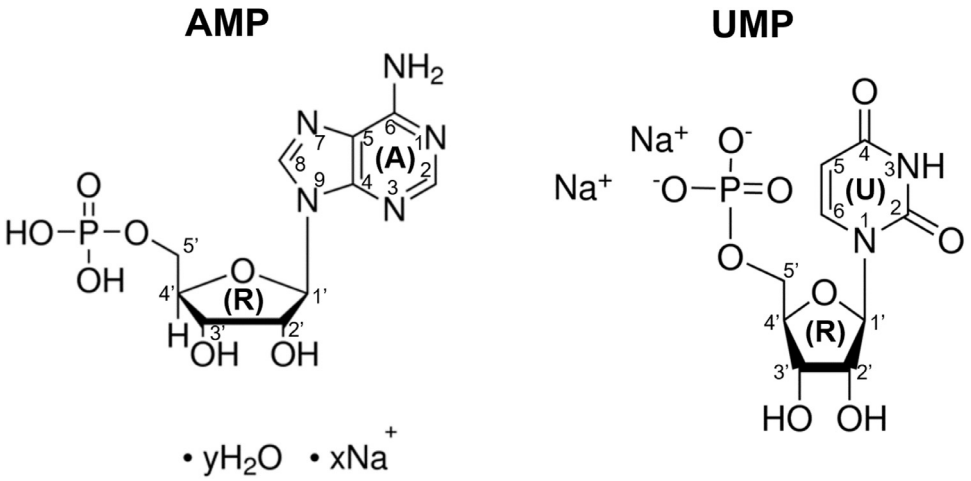

Fig. 1. Structures of adenosine 5′-monophosphate sodium salt (AMP) and uridine 5′-monophosphate disodium salt (UMP) purchased from Sigma-Aldrich. The adenine (A), uracil (U) and ribose (R) moieties are indicated.

Table 1
Type, provenance and chemical composition measured through X-Ray Fluorescence (XRF) of the natural mineral samples employed in this work.

Mineral Sample Provenance Chemical composition	Apatite Morocco %	Labradorite Norway %	Lizardite Finland %	Natrolite Tanzania %	Antigorite Poland %	Forsterite Norway %*
Na_2O		4.1 ± 0.4	0.15 ± 0.03	11.9 ± 0.1	0.12 ± 0.02	
MgO		1.86 ± 0.07	49 ± 5	1.29 ± 0.04	37 ± 4	49.5 ± 0.5
Al_2O_3		28 ± 3	10.6 ± 0.6	32 ± 3	1.87 ± 0.08	0.45 ± 0.05
SiO_2		54 ± 2	35 ± 2	53 ± 3	52 ± 2	41.8 ± 0.2
P_2O_5	40 ± 4	0.010 ± 0.001	0.10 ± 0.01	0.013 ± 0.001		
SO_3	0.19 ± 0.02	0.044 ± 0.007	0.07 ± 0.01	0.051 ± 0.009	0.054 ± 0.009	
K_2O	0.27 ± 0.05	0.73 ± 0.02		0.0061 ± 0.0002		
CaO	59 ± 8	10.61 ± 0.04	0.11 ± 0.01	1.1 ± 0.1	0.010 ± 0.001	
TiO_2	0.07 ± 0.01	0.12 ± 0.02			0.038 ± 0.007	
MnO	0.06 ± 0.02				0.129 ± 0.005	
Fe_2O_3		0.29 ± 0.07	5.3 ± 0.5		8.6 ± 0.9	7.0 ± 0.3
CoO	0.032 ± 0.005				0.012 ± 0.002	
NiO	0.0106 ± 0.0008	0.0012 ± 0.0002	0.018 ± 0.004	0.0045 ± 0.00002	0.242 ± 0.005	0.33 ± 0.03
CuO	0.0061 ± 0.0006	0.0019 ± 0.0002	0.0013 ± 0.0002	0.0019 ± 0.0002	0.0054 ± 0.0006	
ZnO	0.0051 ± 0.0005	0.0018 ± 0.0002	0.0020 ± 0.0002	0.00083 ± 0.00008	0.012 ± 0.003	
Cr_2O_3	0.077 ± 0.003				0.48 ± 0.07	0.25 ± 0.05

* Previously characterized by Fornaro et al. (2013b).

solutions with respect to the typical fluorine-rich apatite of terrestrial basalts and, hence, greater availability of phosphate for prebiotic processes such as the synthesis of activated ribonucleotides (Powner et al., 2009; Szostak, 2009). Apatite is also a biomineral, whose aggregate formation on Earth may result from bacterial decay (Sun et al., 2014).

3. Materials and methods

3.1. Preparation of Mars soil analogues

Adenosine 5′-monophosphate sodium salt (AMP) and uridine 5′-monophosphate disodium salt (UMP) were purchased from Sigma-Aldrich. Structures and numbering schemes for these molecules are shown in Fig. 1.

Regarding mineral samples, only hematite was synthetic, specifically iron(III) oxide powder of 5 µm, also purchased from Sigma-Aldrich. All other mineral samples were natural and were characterized by powder X-Ray Diffraction (XRD) (Bruker D2 Phaser) and X-Ray Fluorescence (XRF) (Ametek SPECTRO XEPOS). Their type, provenance and chemical composition are reported in Table 1. XRD patterns for the natural minerals are also reported in the Electronic Supplementary Information (ESI).

The natural minerals required more treatments to remove organic contaminations. In particular, the mineral samples were crushed into fine powder using a Retsch Planetary Ball Mill PM100, and the mineral powder was sieved in different grain size ranges using a Retsch Vibratory Sieve Shaker AS 200: lizardite, antigorite and labradorite < 20 µm, forsterite in the range 50–100 µm, natrolite in the range 20–200 µm, apatite < 200 µm. Then, to remove organic contaminations, each mineral powder was subjected to repeated washing cycles with methanol/water and sonication. The presence of organics was monitored through infrared spectroscopy before and after the treatments. In the case of forsterite, labradorite and apatite samples, further oxidation of organics with hydrogen peroxide was necessary to remove organics. No modifications of the mineral structures were observed by infrared characterization in the case of the samples treated with hydrogen peroxide.

Once we obtained clean mineral surfaces for biomarker interactions, we prepared Mars soil analogues simulating low-organic content of Martian soil by doping the selected minerals with the nucleotides AMP and UMP.

Two different sample preparation methods were employed, *i.e.* equilibrium adsorption (equilibrium samples) and incipient wet-

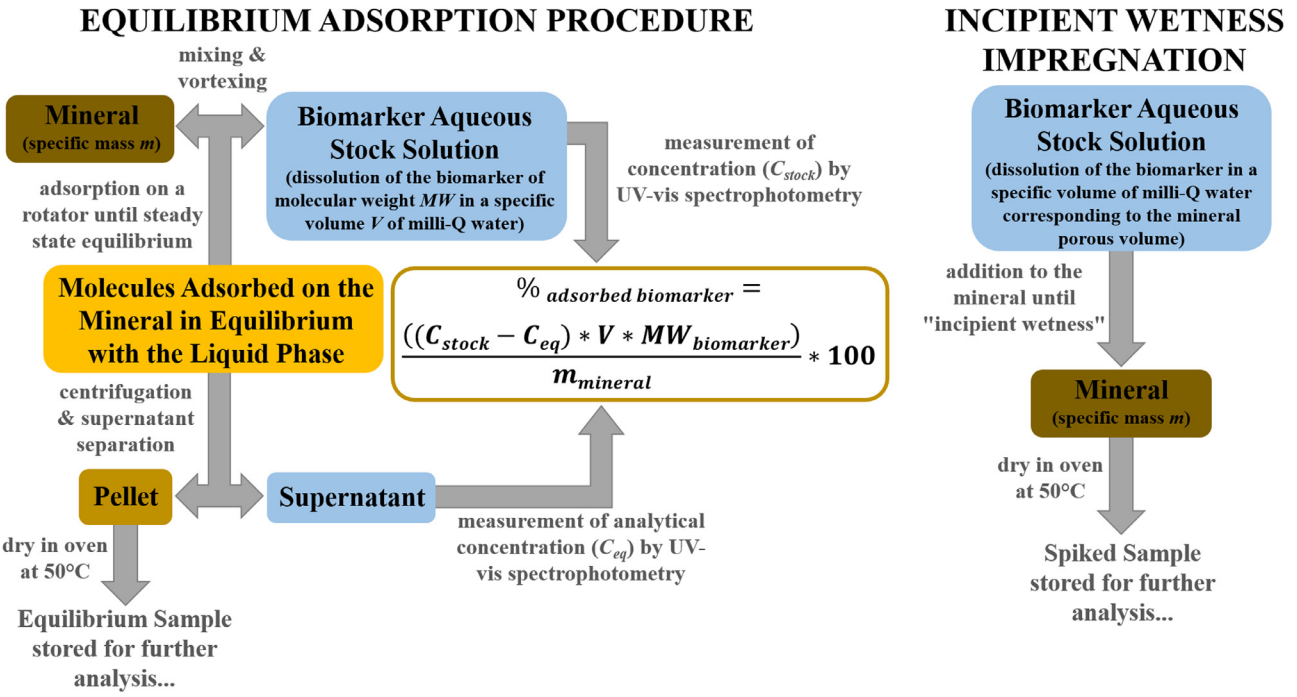

Fig. 2. Scheme of the methods employed for preparation of Mars soil analogues.

ness impregnation (spiked samples), which are schematically represented in Fig. 2 and described as follows.

In the equilibrium adsorption procedure, we firstly prepared 100 mM nucleotide stock solutions by dissolving the appropriate amount of pure nucleotide solid powder in a specific volume of milli-Q water. Then, we mixed the mineral powder with the aqueous stock solution of the biomarker, using a mineral concentration of about 30 g L^{-1}, and we put the suspensions on a test tube rotator for about 24 hours (estimated as a time sufficient to reach steady state equilibrium) upon homogenizing them by vortex. After equilibrium adsorption, we centrifuged the suspensions to pellet suspended mineral particles and separate the supernatant. The analytical concentration of the biomarker was measured both in the stock solutions and supernatants by UV–vis spectrophotometry and the amount of nucleotides adsorbed in equilibrium with the mineral was estimated by subtracting the amount of nucleotides in the supernatant from the total amount of nucleotides initially added. In this way, we estimated an average percentage of adsorbed organics for these samples of about 5%. Finally, we dried pellets in an oven in mild conditions (50 °C) and stored the samples for further studies.

For comparison, we prepared other samples using a water deposition method, namely the incipient wetness impregnation technique. Specifically, we prepared an aqueous solution of the nucleotide and we added it dropwise to the porous solid as long as it filled the porosity at "incipient wetness" and no separate liquid phase was observed. This procedure insures rapid and homogeneous transfer through capillarity forces. To get more homogeneous adsorption, we also vortexed the suspensions. Then, we dried the suspensions in mild conditions (50 °C) without any separation step, so that the total amount of molecules introduced in the aqueous solution remained in the final solid phase, no matter what interaction was established with the surface. We first estimated the porous volume in a separate experiment, adding pure water to the mineral powder until we observed a separate liquid phase. For these samples, we used a molecule-mineral mass ratio of 1:10, obtaining a content of 10% of organics.

Sample were prepared in duplicates, in order to place one under the UV beam and use a second one as dark control not subjected to UV light.

3.2. Characterization of Mars soil analogues

Insights into the specific molecule-mineral interactions were gained by combining complementary techniques such as Time-of-Flight Secondary Ion Mass Spectrometry (ToF-SIMS), Diffuse Reflectance Infrared Fourier Transform Spectroscopy (DRIFTS) and Confocal Raman Imaging Spectroscopy (CRIS).

ToF-SIMS analysis was performed using a facility available at RISE Research Institutes of Sweden in Borås, on a ToF-SIMS IV (ION-TOF GmbH), by mounting the doped mineral samples on double-sticky tape on a silica wafer, and rastering a 25 keV Bi_3^+ beam (pulsed current of 0.1 pA) over an area of ~200 × 200 µm for 200–300 sec. The analyses were performed in positive and negative mode at high mass resolution (bunched mode: Δl ~ 3 µm, m/Δm ~ 2000–4000 at *m/z* 30). Additional analyses were also performed in high spatial resolution mode (0.04 pA, burst alignment mode: Δm/m 100–300, Δl < 1 µm). As a control, additional spectra were also acquired from the tape to confirm that samples were not contaminated by the tape.

DRIFTS measurements were carried out both using a *Vertex 70v* (*Bruker*) FTIR instrument equipped with a *Praying Mantis*™ *Diffuse Reflection Accessory* (*Harrick DRIFT*), and a *Nicolet 6700* FTIR instrument equipped with a diffuse reflection accessory that operates under nitrogen flux. The spectra were recorded in the 4000–400 cm^{-1} spectral range using a DTGS detector and a resolution of 4 cm^{-1}.

Raman spectra and images were collected using a Witec α-Scanning Near-Field Optical Microscope that has been customized to incorporate confocal Raman spectroscopic imaging. Both thin sections and fresh fracture surfaces were examined. The excitation source is a frequency-doubled solid-state YAG laser (532 nm) operating between 0.3 and 1 mW output power (dependent on objective), as measured at the sample using a laser power meter. Objective lenses used included a x100 LWD and a x20 LWD with a 50 µm

optical fiber acting as the confocal pin hole. Spectra were collected on a Peltier-cooled Andor EMCCD chip, after passing through a f/4 300 mm focal length imaging spectrometer typically using a 600 lines/mm grating. The lateral resolution of the instrument is as small as 360 nm in air when using the x100 LWD objective, with a focal plane depth of ~800 nm. This instrument is capable of operating in several modes, and during this study we specifically used imaging in 2D as well as single spectra modes. Single spectra mode allows the acquisition of a spectrum from a single spot on the target. Average spectra were produced typically using integration times between 3 and 30 seconds per accumulation and 10 accumulations to allow verification of weak spectral features. We identified the target areas on the sample powders deposited on a glass slide in transmitted light. The microscope was then switched to reflected light and refocused to the surface. At which point X, Y and Z piezos of the stage were reset. Switching back to transmitted light then allowed an accurate measurement of the depth of the feature of interest. A cosmic ray reduction routine was used to reduce the effects of stray radiation on Raman images, as was image thresholding to reject isolated bright pixels. Fluorescence effects were inhibited by the use of specific peak fitting and flattening.

3.3. UV irradiation experiments

The UV processing of biomarkers included into Martian soil was simulated by performing irradiation experiments in the mid-UV region of the Mars soil analogues prepared in the laboratory.

Two different set of experiments were performed: (i) *in situ* UV irradiation under terrestrial ambient temperature and pressure by using an experimental setup assembled at INAF-Astrophysical Observatory of Arcetri (Florence, Italy), which allows monitoring *in situ* the degradation process by infrared spectroscopic analysis; (ii) *ex situ* UV irradiation under Martian-like conditions of 6 mbar carbon dioxide atmosphere and nominal temperature −20 °C inside the PALLAS (Planetary Analogues Laboratory for Light, Atmosphere, and Surface Simulations) chamber developed at Utrecht University (The Netherlands), which is a new facility specifically designed to simulate planetary (sub)surface conditions on rocky bodies in the solar system (ten Kate and Reuver, 2016).

3.3.1. In situ UV irradiation experimental setup

The *in situ* UV irradiation experimental setup is constituted by a Newport Oriel 300 W Xenon arc discharge lamp (spectral range 200–930 nm) whose light is focused directly on the sample through an optical fiber of 800 µm spot size. With this setup, the irradiated spot of the sample presents an area of 7.07 mm^2 and the UV flux focussed on the sample is 2.75×10^{17} photons s^{-1} cm^{-2} in the 200–400 nm spectral range, as measured through a single monochromator Spectro 320 scanning spectrometer (Instrument System).

The optical fiber is inserted into the sample chamber of a single beam double pendulum interferometer *Vertex 70v* (*Bruker*), equipped with a *Praying Mantis*™ *Diffuse Reflection Accessory* (*Harrick DRIFT*) (Fig. 3). This configuration allows *in situ* spectroscopic characterization using DRIFTS.

In order to monitor the photodegradation, infrared spectra were recorded at regular intervals during UV irradiation for a total time of about 20 hours. This procedure allowed us to follow the degradation process in real time and possibly the formation of new species by observing changes in the infrared spectroscopic features.

We investigated the degradation kinetics by evaluating the decrease rate of the intensities of the infrared bands attributable to the molecules adsorbed on the minerals. Indeed, the area of such bands may be considered proportional to the number of molecules and calculated by integrating the spectrum between two arbitrary integration limits. The degradation rate β for a given band can be obtained by fitting the fraction of unaltered molecules $\frac{N(t)}{N_0}$, estimated by the area of the band at a specific time normalized on the area of the same band pre-irradiation, *vs.* time, using a first-order kinetics function:

$$\frac{N(t)}{N_0} = B \times e^{-\beta t} + C \quad (1)$$

where N_0 is the initial number of molecules in the sample, B is the fraction of molecules that interact with UV radiation and C is the fraction of molecules that do not interact with UV radiation due to, for example, their position in the inner part of the solid samples. The C factor accounts for the fact that infrared radiation can penetrate much deeper into the solid sample with respect to UV radiation and the infrared spectrum is the result of both the inner (not UV-irradiated) part of the sample and the superficial UV-irradiated one.

In the case of formation of new peaks, the kinetics can be investigated through the function:

$$N_f(t) = N_{f0} \times \left(1 - e^{-\alpha t}\right) \quad (2)$$

where $N_f(t)$ is the number of molecules formed at time t, N_{f0} is the maximum number of molecules formed and α is the formation rate.

For a first-order kinetics the half-lifetimes (time required to destroy 50% of the initial material) can be obtained as $t_{\frac{1}{2}} = \frac{\ln(2)}{\beta}$.

Furthermore, the UV destruction cross-section σ, which represents the probability of interaction between molecule and UV radiation, can be derived from $\beta = \sigma \times \phi$, where ϕ is the incident flux of UV photons per area unit. In the same way the formation cross-section σ_f can be estimated from $\alpha = \sigma_f \times \phi$. Once σ in our laboratory conditions is calculated, it is possible to derive the half-lifetimes experienced under the Martian UV flux estimated by Patel et al. (2002) as 1.4×10^{15} photons s^{-1} cm^{-2} in the 190–325 nm spectral range.

3.3.2. Ex situ UV irradiation experimental setup

Ex situ UV irradiation experiments were performed in PALLAS, a recently established planetary surface simulation facility (ten Kate and Reuver, 2016). PALLAS (Fig. 4A) is a 50 × 50 × 50 cm stainless steel vacuum chamber (Pfeiffer Vacuum) equipped with various ports and windows, and a large door for sample access. A differentially pumped sampling volume, the atmospheric sample chamber (ASC), is mounted onto the main chamber and connected via both a gate valve and a needle valve. The ASC is equipped with a turbo pump (Pfeiffer Vacuum Turbo HiPace 80) attached to a diaphragm pump (Pfeiffer Vacuum MVP 070–3), a mass spectrometer (Pfeiffer Vacuum QMG 220 M1, PrismaPlus Compact) and a pressure gauge (Pfeiffer Vacuum PKR251, 10^{11}– 1100 mbar). The entire system (chamber + ACS) can be pumped down to pressures around 10^{-8} mbar through the gate valve. Samples were irradiated with a Xenon arc discharge lamp (LOT-Oriel, 450 W UV enhanced Xe, 180–900 nm) under simulated Martian conditions, specifically an average (nominal) temperature of −20 °C, maintained by a JULABO FP89-AL ultra-low refrigerated heating circulator, and a 6-mbar atmosphere of carbon dioxide for 40 hours. The UV flux for this lamp, measured in vacuum inside the PALLAS chamber using an Ocean Optics Maya2000Pro UV spectrometer, is 5.42×10^{18} photons s^{-1} cm^{-2} in the 200–400 nm spectral range.

The experimental protocol was as follows. Samples were placed inside stainless steel sample holders on a cooling table with an aluminium foil separating the irradiated samples from the dark controls, which were placed under an aluminium cup as shown in Fig. 2B. Then, the chamber was closed and carefully pumped down through either the gate valve or the needle valve. When the

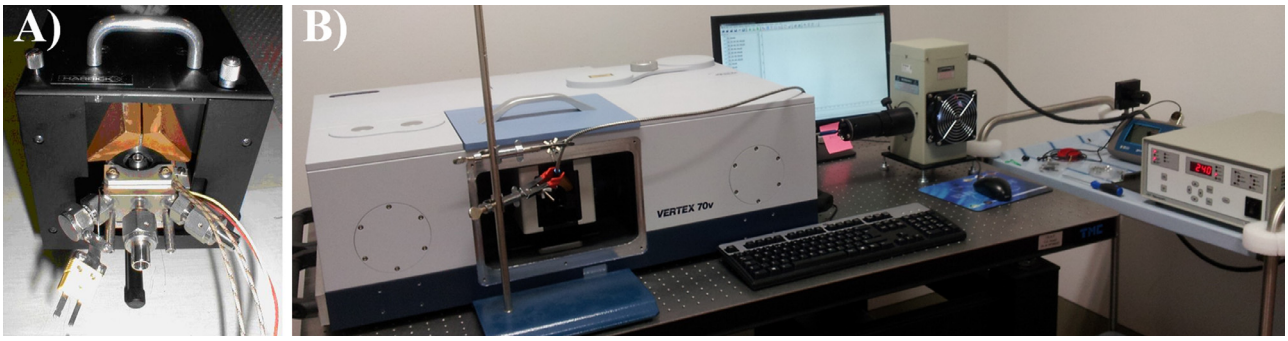

Fig. 3. A) Praying Mantis™ Diffuse Reflection Accessory and reaction chamber. **B)** Experimental setup used for *in situ* UV irradiation experiments.

Fig. 4. A) PALLAS chamber used for UV irradiation experiments under Marian-like conditions, equipped with an atmospheric sample chamber attached to a mass spectrometer (on the right of the chamber) and a xenon arc discharge lamp (on the top of the chamber). **B)** Sample holders placed inside the chamber on a cooling table, connected to an ultra-low refrigerated heating circulator, separated through an aluminium foil by dark controls placed under an aluminium cup. We measured the temperature on the cooling table using thermocouples connected to a voltmeter.

pressure inside the chamber reached at least 10^{-7} mbar, a background mass spectrum was recorded to monitor the atmospheric gases present in the chamber. When both background and pressure requirements were met, both the gate valve and the needle valve were closed and the chamber was filled with the desired atmosphere. The chamber pressure was monitored on the chamber pressure gauge (Pfeiffer Vacuum CMR361, 0.1–1100 mbar). The ASC was continuously pumped. To carry out atmospheric analyses a little gas was let into the ACS up to pressures of around 10^{-6} mbar.

DRIFTS measurements were carried out pre- and post-irradiation through the *Nicolet 6700* FTIR instrument equipped with a DRIFTS accessory.

4. Results and discussion

4.1. Characterization of Mars soil analogues and study of molecule–mineral interactions

In the ToF-SIMS spectra of all minerals with absorbed AMP at equilibrium, we observed fragment ions (*m/z* 136.06, $C_5H_6N_5$ and *m/z* 158.05, $C_5H_5N_5Na$) and pseudo-molecular ions from AMP (*m/z* 392.03, $C_{10}H_{13}N_5O_7PNa_2$). The pseudo-molecular ions were very weak in the spectra of the silicates while much stronger in the spectra of apatite and hematite. ToF-SIMS ion images showed the distribution of different molecules/elements across the scanned surface (200 µm × 200 µm). In particular, AMP appeared to be relatively homogenously distributed over the mineral surfaces in the case of apatite and hematite. For all silicates, instead, we observed a heterogeneous spatial distribution of AMP, with spots of tens of microns where the intensity of the ion signals originating from AMP was very low or absent while the ion signals from the mineral were very intense. This indicates that AMP does not adsorb homogeneously on the surfaces of forsterite, natrolite, labradorite, lizardite and antigorite, despite the assumption that the equilibrium adsorption method is supposed to be the best for maximizing molecular homogeneity through the mineral samples. As case study, we show in Fig. 5 the ToF-SIMS ion images for AMP adsorbed on apatite (homogeneous spatial distribution of molecules) and AMP adsorbed on lizardite (heterogeneous spatial distribution of molecules).

In the ToF-SIMS spectra of the minerals with absorbed UMP at equilibrium, we observed only weak fragment ions, such as *m/z* 113.04 ($C_4H_4N_2O_2H$) and 135.02 ($C_4H_4N_2O_2Na$), except for the hematite sample for which we detected also a strong pseudo-molecular ion at *m/z* 369.01 ($C_9H_{12}N_2O_9PNa_2$). For all minerals except apatite, the ion signals from UMP were quite evenly distributed across the surface. However, it is important to note that for samples doped with UMP, the signals were generally weaker than samples doped with AMP, which makes unambiguous interpretation of the data more difficult.

We used infrared (DRIFTS) and Raman (CRIS) vibrational spectroscopies to characterize at the molecular level the nature of the interactions between molecules and mineral surface sites by observing vibrational shifts and changes in the intensity of the bands with respect to the pure molecules and minerals, whereby it is possible to deduce the molecular functional groups and the surface sites involved in the molecule-mineral interactions.

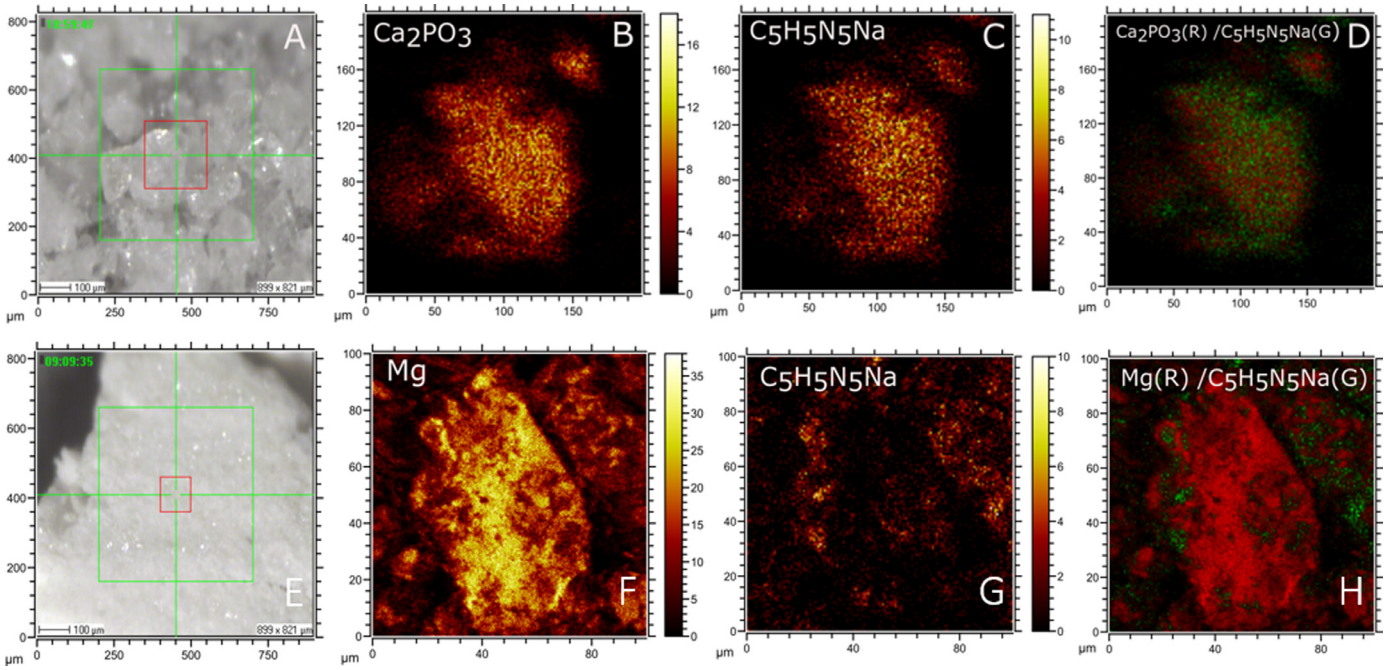

Fig. 5. Positive ToF-SIMS images obtained for the sample of AMP adsorbed on apatite at equilibrium (**A-D**) and AMP adsorbed on lizardite at equilibrium (**E-H**). AMP adsorbed on apatite: **A)** ToF-SIMS video image, where the red square indicates the area of ToF-SIMS analysis shown in **B-D; B)** ToF-SIMS ion image of $Ca_2PO_3^+$originating from the mineral apatite; **C)** ToF-SIMS ion image of $C_5H_5N_5Na^+$ fragment ion of the nucleotide AMP; **D)** Composite ion image of **B** (red) and **C** (green). AMP adsorbed on lizardite: **E)** ToF-SIMS video image, where the red square indicates the area of ToF-SIMS analysis shown in **F-H; F)** ToF-SIMS ion image of Mg^+ originating from the mineral lizardite; **G)** ToF-SIMS ion image of $C_5H_5N_5Na^+$ fragment ion of the nucleotide AMP; **H)** Composite ion image of **F** (red) and **G** (green). (For interpretation of the references to colour in this figure legend, the reader is referred to the web version of this article.)

Table 1s in the ESI reports the infrared vibrational frequencies for the pure nucleotides compared with the values for nucleotides adsorbed on the different minerals. From the infrared data shown in Table 1s, we can infer that in all equilibrium samples AMP interacts through the amino group of the adenine moiety, whose scissoring modes undergo red-shifts with respect to the pure AMP for most of the minerals, except for the natrolite sample where a blue-shift is observed instead. The infrared bands corresponding to the stretching modes of the phosphate groups are weakly observed only in the case of the hematite sample, whose vibrational shifts point to the involvement of the phosphate in the molecule-mineral interactions. In the case of UMP equilibrium samples, infrared outcomes clearly show the involvement of the carbonyl group of the uracil moiety for the lizardite, labradorite and apatite samples, while for forsterite, natrolite, antigorite and hematite, vibrational shifts are mainly observed for the C–H bending modes of the ribose moiety, whereby we can deduce that the ribose moiety mainly interacts with surface sites for those samples.

As case study, we examined in more detail the vibrational features of AMP adsorbed on lizardite (heterogeneous spatial distribution of molecules) and apatite (homogeneous spatial distribution of molecules) both with DRIFTS (Fig. 6) and CRIS (Fig. 7 and 8).

From the infrared vibrational shifts of AMP bands shown in Fig. 6, we deduce that for both lizardite and apatite samples AMP interacts with the mineral surface through the amino group of the adenine moiety because its vibrational scissoring modes undergo red-shifts of −10/−20 cm^{-1}. These small red-shifts and the absence of new infrared bands suggest the involvement of weak physical interactions, excluding instead the formation of hydrogen bonds or covalent bonds with the mineral surface through the amino group of the adenine residue. In fact, previous studies show that direct hydrogen bonds through the amino group should result in more remarkable red-shifts of the scissoring mode of about −70 cm^{-1} (Fornaro et al., 2014, 2016).

Regarding the phosphate group of AMP, we could not examine its involvement in the interactions with the mineral surface sites from the infrared data because the infrared bands of the minerals cover its stretching mode at about 800 cm^{-1}.

However, we gained complementary information for investigating molecule-mineral interactions through confocal micro-Raman imaging. Spectral imaging allowed us to detect the molecules even in the case of heterogeneous spatial distribution, by acquiring Raman maps across a large area of the sample and scanning the map in order to find the molecular features. Once we found the spots where the molecules were localized, we focused on these spots and acquired single spectra with longer integration times (the black spectra shown in Figs. 7 and 8 for AMP adsorbed on lizardite and apatite, respectively).

Specifically, from the comparison shown in Fig. 7C between the Raman spectra of AMP adsorbed on lizardite and the spectra of pure AMP and untreated lizardite mineral, we can infer that AMP interacts through its phosphate group with hydroxyl surface groups. Indeed, the symmetric stretching of the phosphate group of AMP splits and the stretching of the hydroxyl groups of lizardite decreases due to the formation of covalent bonds with the phosphate group. The splitting indicates lowering of symmetry due to chemisorption, which determines a breakdown of selection rules. New peaks for the stretching of the hydroxyl groups of lizardite appear due to the change in the surface environment as consequence of chemisorption. In the Raman spectra we could not analyse the changes in the vibrational modes of the amino group of the adenine moiety due to its low Raman scattering, but combining IR and Raman experimental outcomes we obtained complementary information indicating the formation of surface complexes in which AMP molecules interact with the hydroxyl surface sites both through covalent bonds involving the phosphate group and hydrogen bonds involving the amino group of the adenine moiety.

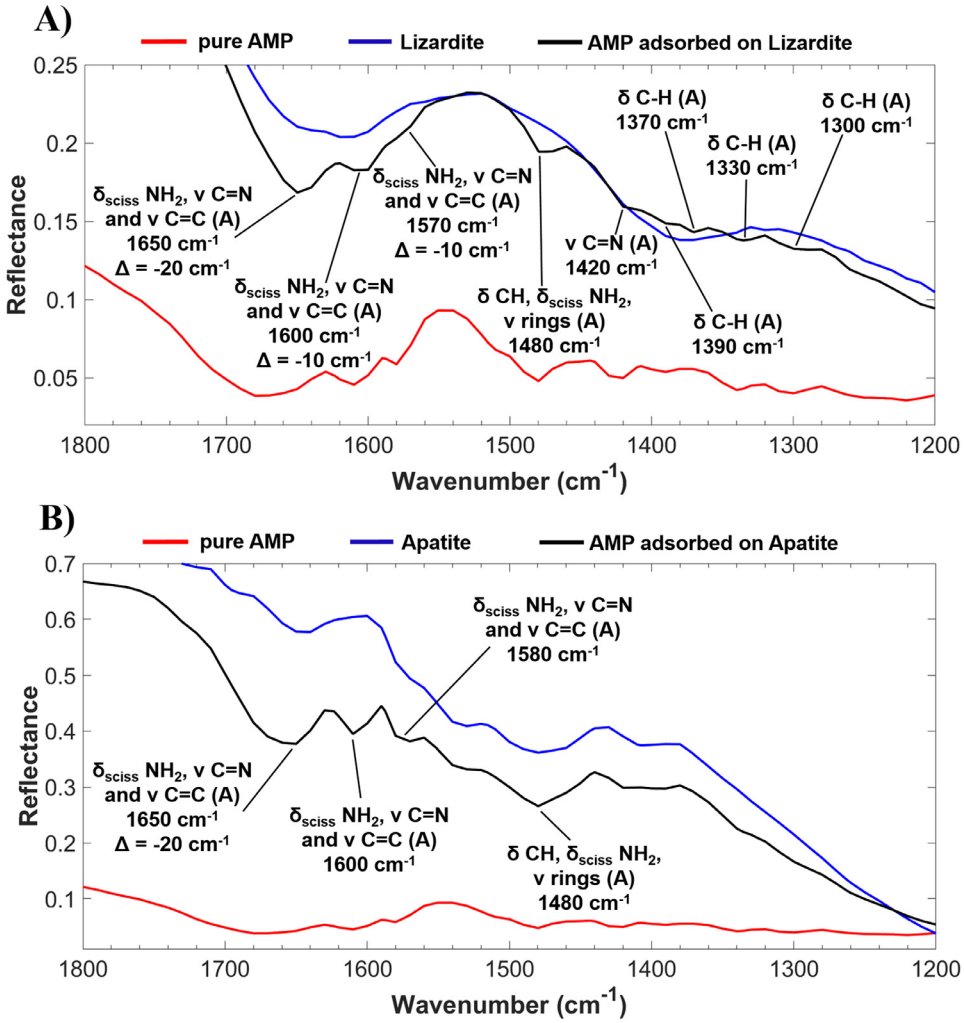

Fig. 6. A) Infrared spectra of pure AMP (red), pure lizardite (blue) and AMP adsorbed on lizardite at equilibrium (black), along with the shifts of vibrational frequencies of AMP adsorbed on lizardite with respect to pure AMP (Δ). **B)** Infrared spectra of pure AMP (red), pure apatite (blue) and AMP adsorbed on apatite at equilibrium (black), along with the shifts of vibrational frequencies of AMP adsorbed on apatite with respect to pure AMP (Δ). Assignment of vibrational modes based on Fornaro et al. (2018) and Tsuboi (1970). Abbreviations: ν = stretching; δ = bending; sciss = scissoring. (For interpretation of the references to colour in this figure legend, the reader is referred to the web version of this article.)

Previous studies suggest that phosphate groups tend to form covalent bonds with metal-hydroxyls mineral sites through ligand exchange (Banin et al., 1985; Hashizume et al., 2010; Pedreira-Segade et al., 2016). Pedreira-Segade et al. (2016) studied adsorption of nucleotides on lizardite and suggested that ligand exchange between the phosphate group of nucleotides and the metal hydroxyls of the broken edges of the phyllosilicates is the main adsorption mechanism at neutral pH at low surface loadings. Cation exchange, instead, should be significant only at acidic pH conditions since for most pH values there is a global electrostatic repulsion between charged particles and nucleotides. In our adsorption experiments of AMP on lizardite, equilibrium pH is 7.28. At this pH value, AMP molecules are in the anionic forms and the surface of lizardite is negatively charged because the point of zero charge for this mineral is around pH 3. Therefore, we can rule out the involvement of any electrostatic attraction in the adsorption mechanism, while ligand exchange appears to be the most likely process.

The Raman data for AMP adsorbed on apatite, shown in Fig. 8, point to the involvement of the adenine moiety in the interaction with the mineral, in agreement with the previous infrared outcomes and Hammami et al. (2015). Differently from AMP adsorbed on lizardite, we did not observe any significant Raman band for the stretching motion of the phosphate group of AMP adsorbed on apatite (only a very weak signal at 1030 cm^{-1}). This may be ascribed to the relatively low-energy interaction between AMP and apatite, estimated by Hammami et al. (2015) as −22 kJ/mol, which is consistent with the typical strength of an electrostatically-mediated interaction intermediate between physisorption and chemisorption. At the equilibrium pH 5.53 measured in our experiments for adsorption of AMP on apatite, the mineral surface develops positive charges (the point of zero charge for apatite is around pH 8), while AMP molecules are negatively charged. Therefore, we can expect that electrostatic interactions play a role in the adsorption mechanism by favoring concentration of the polarizable AMP anions in the hydration shell of apatite thanks to charge neutralization. Weak adsorption to the crystal surface may also occur at the high molecular concentration used in our experiments, in agreement with the results reported by Burton et al. (1969). Both Hammami et al. (2015) and Hermes-Lima et al. (1990) reported adsorption isotherms for AMP on apatite characterized by a sigmoidal profile indicative of a cooperative molecular association, which can likely occur through self-stacking interactions of the adenine residues (Yamauchi et al., 1996).

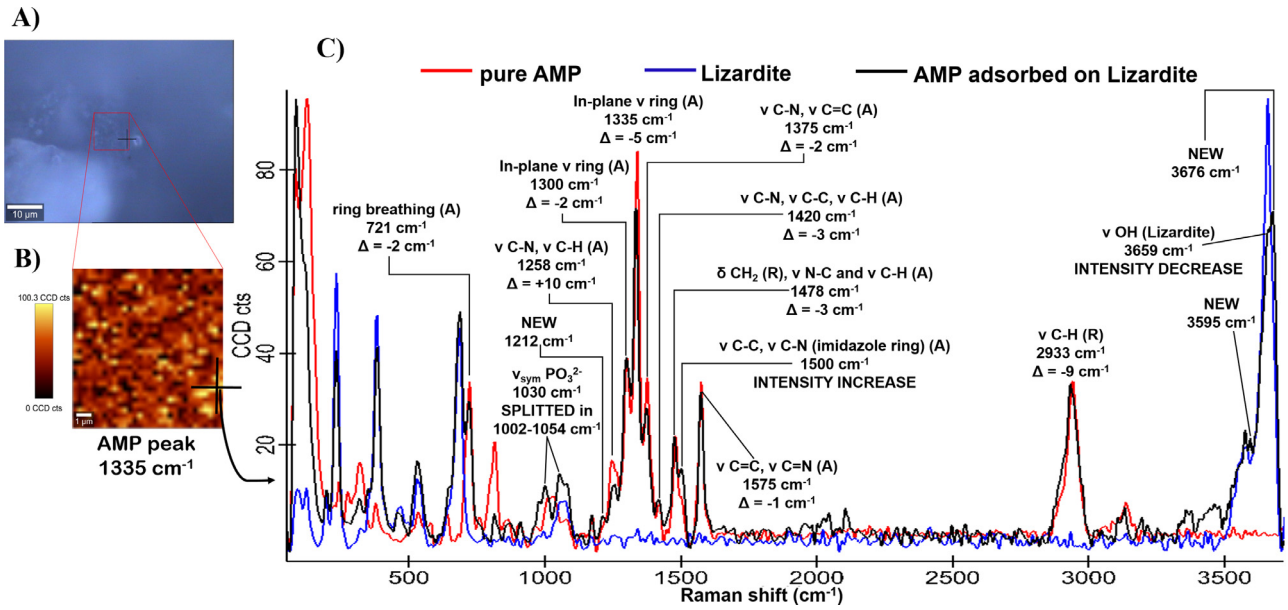

Fig. 7. A) Visible image of the sample, highlighting in the red square the portion of the sample under investigation. **B)** Spatial distribution of the peak of AMP at 1335 cm^{-1}. **C)** Raman spectra of pure AMP (red), pure lizardite (blue) and AMP adsorbed on lizardite at equilibrium (black), along with the shifts of vibrational frequencies of AMP adsorbed on lizardite with respect to pure AMP (Δ). Assignment of vibrational modes is based on Kundu et al. (2009), Lang et al. (2011), Ostovarpour and Blanch (2012). Abbreviations: ν = stretching; δ = bending; sym = symmetric. (For interpretation of the references to colour in this figure legend, the reader is referred to the web version of this article.)

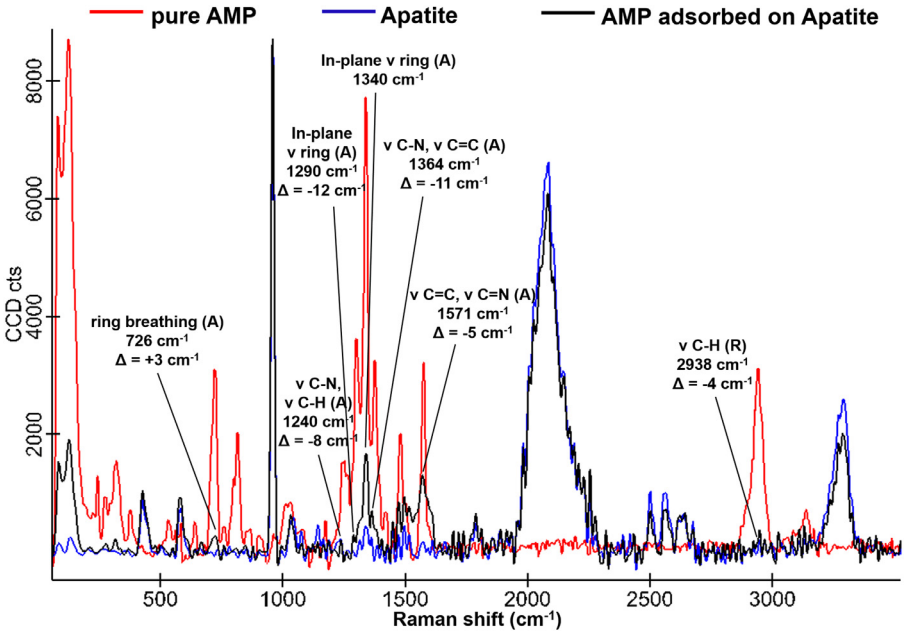

Fig. 8. Raman spectra of pure AMP (red), pure apatite (blue) and AMP adsorbed on apatite at equilibrium (black), along with the shifts of vibrational frequencies of AMP adsorbed on apatite with respect to pure AMP (Δ). Assignment of vibrational modes is based on Kundu et al. (2009), Lang et al. (2011), Ostovarpour and Blanch (2012). Abbreviations: ν = stretching; δ = bending; sym = symmetric. (For interpretation of the references to colour in this figure legend, the reader is referred to the web version of this article.)

In conclusion, our analyses point out that ToF-SIMS, Raman and infrared spectroscopies are very sensitive complementary techniques to investigate molecule-mineral interactions and for detection of biomarkers features.

4.2. UV irradiation

The destruction cross-sections σ, the formation cross-sections σ_f, and the half-lifetimes relative to the Martian UV flux $t_{1/2}$ Mars obtained from *in situ* UV irradiation experiments in ambient terrestrial conditions for each detectable infrared peak of AMP and UMP, both pure and adsorbed at equilibrium on lizardite, are reported in detail in Table 2s of the ESI. Table 2 summarizes the weighted average values obtained by fitting the degradation data for all detectable infrared peaks of AMP and UMP, along with the formation cross-sections σ_f of peaks forming during *in situ* UV irradiation experiments in terrestrial ambient conditions.

In the case of *ex situ* UV irradiation experiments performed inside PALLAS chamber under simulated Martian conditions, infrared characterization was performed just before and after UV process-

Table 2
Weighted average destruction cross-sections σ and relative half-lifetimes under Martian UV flux $t_{1/2\ Mars}$ for all detectable infrared peaks of AMP and UMP, along with the formation cross-sections σ_f of peaks forming during *in situ* UV irradiation experiments in terrestrial ambient conditions (denoted by an asterisk).

Peak (cm^{-1})	σ (cm^2)	$t_{1/2\ Mars}$ Martian days	σ_f (cm^2)
AMP			
weighted average of all detectable peaks	$(1.4 \pm 0.1) \times 10^{-22}$	27 ± 2	
AMP adsorbed on Lizardite			
2164*			$(9 \pm 1) \times 10^{-23}$
1600	$(2.2 \pm 0.6) \times 10^{-22}$	26 ± 8	
UMP			
weighted average of all detectable peaks	$(1.05 \pm 0.03) \times 10^{-22}$	35.4 ± 0.8	
673*			$(1 \pm 2) \times 10^{-23}$
UMP adsorbed on Lizardite			
2164*			$(1.3 \pm 0.2) \times 10^{-22}$

ing. Therefore, it was not possible to follow the degradation kinetics and fit the data. The same exponential formula of Eq. (1) was applied to derive estimates of the cross-sections and half-lifetimes of degradation under simulated Martian conditions as well.

Table 3s of the ESI reports in detail the percentages of degradation after 40 hours of UV irradiation of the equilibrium samples inside the PALLAS chamber for each detected infrared peak of the nucleotide, which are obtained as $\%\ deg = (A_{pre} - A_{post}) \times 100/A_{pre}$, where A_{pre} is the area of the peak pre-irradiation and A_{post} is the area of the peak post-irradiation. Table 3 reports just the percentages of degradation for the most relevant infrared peaks, along with the assignments of vibrational modes (Fornaro et al., 2018; Leulliot et al., 1999; Tsuboi, 1970).

Possible catalytic or protective effects of minerals can be evaluated by comparing the degradation kinetics of analogous infrared peaks in the case of the pure molecule and the molecule adsorbed on the mineral. In this work, we define the degrading power of the mineral as the average percentage of degradation for all the peaks of the nucleotide detectable on the mineral evaluated relative to the degradation of the analogous peaks of the pure nucleotide in 40 hours of UV irradiation under Martian-like conditions inside the PALLAS chamber. More precisely, to evaluate the degrading power of a mineral, we subtracted the percentage of degradation observed in 40 hours of UV irradiation under Martian-like conditions for each detectable peak of the nucleotide in the presence of the mineral to the percentage of degradation for the same peak in the case of the pure nucleotide, and then we took an average for all the detectable peaks. Table 4 reports the power of the different minerals for degrading AMP and UMP in 40 hours of UV irradiation under Martian-like conditions and the average estimates of degradation cross-sections and half-lifetimes. The degrading powers of the different minerals with respect to the pure molecules are also represented in the form of a histogram in Fig. 9 as visual aid for the discussion. Duplicate experiments were performed estimating errors within 20% of the values for samples doped with AMP and 30% for samples doped with UMP.

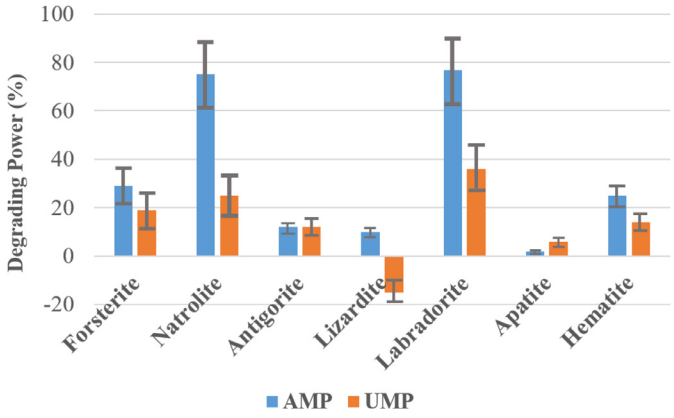

Fig. 9. Power of the different minerals for degrading AMP and UMP in 40 hours of UV irradiation under Martian-like conditions with respect to the degradation of the pure molecules. Error bars are within 20% of the values for samples doped with AMP and 30% for samples doped with UMP. (For interpretation of the references to colour in this figure legend, the reader is referred to the web version of this article.)

4.2.1. Degradation of pure nucleotides

During UV irradiation under ambient conditions, *i.e.* in the presence of atmospheric oxygen at room temperature, we did not observe remarkable changes or the formation of new peaks in the infrared spectrum of pure AMP. The weighted average degradation cross-section for AMP, estimated by fitting the degradation data for all detectable nucleotide bands using Eq. (1), was $(1.4 \pm 0.1) \times 10^{-22}$ cm^2 (detailed data are reported in Table 2), which corresponds to a half-lifetime of about 30 Martian days under Martian UV flux.

UMP showed similar stability in the presence of UV radiation, with degradation cross-section of $(1.05 \pm 0.03) \times 10^{-22}$ cm^2, even though in the case of UMP the changes in the infrared spectra were more remarkable, with formation of a new peak at 673 cm^{-1} and the splitting of the peak at 661 cm^{-1} into the 664 and 654 cm^{-1} peaks (Fig. 10). For the new peak at 673 cm^{-1} appearing during UV irradiation of pure UMP, we used Eq. (2) to estimate a formation cross-section of the order of 10^{-23} cm^2. These changes in the spectral region of the out-of-plane vibrational motion of the N3-H group of the uracil moiety may be attributed to the formation of a cis-syn cyclobutane uracil dimer, which appears to be the main photoproduct of UV irradiation of uracil in the frozen state, in solution or in polynucleotides, arising from the [2 + 2] cycloaddition of the C5 = C6 double bonds of adjacent pyrimidine bases (Shetlar and Basus, 2011). Indeed, the infrared spectrum of the cis-syn cyclobutane uracil dimer presents two intense infrared bands in the 700–650 cm^{-1} spectral region (Varghese, 1971) that can be assigned to the N3-H out-of-plane bending vibrations. This evidence is consistent with our previous study of UV irradiation of nucleobases in vacuum (Fornaro et al., 2013b); indeed, through a re-evaluation of the changes observed in the infrared spectra of uracil during UV irradiation, we denoted also in such a case the appearance of photoproduct marker bands that can be ascribed to the formation of a cis-syn cyclobutane uracil dimer. Consistently with studies reported in the literature (Fornaro et al., 2013b), adenine is more stable in the presence of UV radiation thanks to its electronic structure, which determines an extremely efficient relaxation of the excited state (Nir et al., 2001), and proves more resistance to oxidation (Ravanat et al., 2001). The photodynamics of the pyrimidine bases is much richer and the deactivation time from the excited state to the ground state is also much longer as compared to the purine bases, increasing the probability of photochemical reactions (Barbatti et al., 2010).

Table 3
Percentages of degradation (% deg) after 40 hours of UV irradiation inside the PALLAS chamber under simulated Martian conditions for some relevant infrared peak of AMP and UMP, both pure and adsorbed on the different minerals forsterite, natrolite, antigorite, lizardite, labradorite, apatite and hematite through equilibrium adsorption.

Assignment*	Peak (cm^{-1})	% deg	Peak (cm^{-1})	% deg	Peak (cm^{-1})	% deg	Peak (cm^{-1})	% deg	Peak (cm^{-1})	% deg	Peak (cm^{-1})	% deg	Peak (cm^{-1})	% deg	Peak (cm^{-1})	% deg
	AMP		Forsterite + AMP		Natrolite + AMP		Antigorite + AMP		Lizardite + AMP		Labradorite + AMP		Apatite + AMP		Hematite + AMP	
ν NH_2 (A)	3330 m	21	3330	54							3330	98				
ν C–H (A)	3140 s	10	3140	13			3190	6			3140	95	3140	5		
ν C–H (R)	2940 m	0	2940	0			2940	0	2940 vw	0	2940	98	2940	0		
ν C–H (R)	2880 m	0	2880	0			2900	0	2880 vw	0	2880	98	2880	0		
ν C–H (R)	2720 m	0	2720 w	50							2720	99	2720	0		
δ_{sciss} NH_2, ν C=N, ν C=C (A)	1670 vs	0	1670	13	1690 vw	100	1640	0	1650	0	1650	83	1650	0	1650	0
δ_{sciss} NH_2, ν C=N, ν C=C (A)	1610 s	0	1600	28			1600	59	1600	15	1600	97	1610	4	1600	0
δ_{sciss} NH_2, ν C=N, ν C=C (A)	1580 s	0	1580	8	1580 vw	100			1570	30	1580	0	1580	8	1580	40
δ C–H, δ_{sciss} NH_2, ν rings (A)	1480 s	0	1480	18	1480 vw	36	1480	15	1480	0	1480	95	1480	0	1480	0
δ C–H (R)					1450 vw	100										
ν C=N (A)	1420 s	0	1420	9	1420 vw	72	1420	5	1420 w	22	1420	3			1420	46
δ C–H	1390 m	0	1390 w	100	1390 vw	18			1390 vw / 1370 vw						1370 w	
δ C–H	1330 ms	3	1330 w	12	1340 vw	78			1330 vw						1330	0
δ C–H	1300 ms	18	1300 vw	100	1310 vw	96			1300 vw						1290 w	0
δ C–H	1240 sh														1250 w	70
δ C–H, δ O–H (R), ν P=O	1210 mw	29													1210	62
ν C–O (R)	1080 w		1030	0											1070	0
ν_{asym} P-OH	874 w	0													910 vw	
ν_{sym} P-OH	820 mw	0													800 vw	
	UMP		Forsterite + UMP		Natrolite + UMP		Antigorite + UMP		Lizardite + UMP		Labradorite + UMP		Apatite + UMP		Hematite + UMP	
ν N–H (U)	3000 mw	0	3000 w	34							3000	50	3000	0	3000	27
ν C–H (R)	2880 mw	0	2880 w	40							2880	31	2880	2	2880	25
ν C–H (R)	2780 mw	0	2780 w	99							2780	42	2780	4	2780	40
ν C–H (R)	2670 mw	0	2670 w	87							2670	100	2670	23		
ν C=O (U)	1700 s	0	1700	0			1700	0	1690 w	12	1690	0	1690	0	1700	0

(*continued on next page*)

Table 3 (*continued*)

Assignment*	Peak (cm^{-1})	% deg	Peak (cm^{-1})	% deg	Peak (cm^{-1})	% deg	Peak (cm^{-1})	% deg	Peak (cm^{-1})	% deg	Peak (cm^{-1})	% deg	Peak (cm^{-1})	% deg	Peak (cm^{-1})	% deg
	UMP		Forsterite + UMP		Natrolite + UMP		Antigorite + UMP		Lizardite + UMP		Labradorite + UMP		Apatite + UMP		Hematite + UMP	
ν C=C (U)	1630 sh	69							1630 w	13	1620 vw	100				
δ C–H (R)	1520 w	0			1520 vw	32	1500 vw		1500 w	0					1520	0
ν C–C, C–N (U), δ_{sciss} C5'H_2 (R)	1470 s	0	1470	0	1480 vw	14	1470 w	0	1470 vw		1470	0	1470	0	1470	11
δ C–H (R)	1430 m	65	1430 w	12	1440 vw	100	1440 w	100			1430	100	1430	79	1430	96
δ O–H, δ C–H (R)	1400 m	0	1390 w	0	1400 vw	0							1400	0	1390	0
δ C–H (R)	1340 s	0	1340 w	2	1350 vw	31							1340	12	1340 w	48
δ C–H (R)	1270 s	0	1270 w	0	1270 vw	39			1270 vw						1270	21
δ C–H, δ O–H (R)	1100 m	40													1100	4
ν ring (R)	1050 w		1030	0												
ν ring (U, R), ν N–H (U)	978 s	0													978	0
γ N3-H (U)	661 w						665 vw		665 vw		663 vw					
τ C–O (R), ring def (U)	565 s	0					550 vw				560 vw					
δ_{rock} C5'H_2 (R)	540 vw						540 vw		546 vw							

Abbreviations: ν = stretching; δ = in-plane bending; γ = out-of-plane bending; sciss = scissoring; rock = rocking; asym = asymmetric; sym = symmetric; def = deformation; A = adenosine moiety; U = uracil moiety; R = ribose moiety; s = strong; m = medium; w = weak; vw = very weak; sh = shoulder.

* Assignments based on Fornaro et al. (2018), Leulliot et al. (1999), and Tsuboi (1970).

Table 4
Power of the different minerals for degrading AMP and UMP in 40 hours under Martian-like conditions inside the PALLAS chamber in the case of equilibrium samples, evaluated as the average percentage of degradation for all the peaks attributable to the nucleotide in the presence of the mineral relative to the degradation of the analogous peaks of the pure nucleotide, and average estimates of degradation cross-sections σ and half-lifetimes $t_{1/2\ Mars}$ under Martian flux for all detectable nucleotide peaks.

	Degrading power (%)	Average σ (cm^2)	Average $t_{1/2\ Mars}$ (Martian days)
AMP			
Forsterite	29	4×10^{-25}	10,000
Natrolite	75	2×10^{-24}	3000
Antigorite	12	2×10^{-25}	30,000
Lizardite	10	1×10^{-25}	40,000
Labradorite	77	2×10^{-24}	3000
Apatite	2	3×10^{-26}	200,000
Hematite	25	4×10^{-25}	15,000
UMP			
Forsterite	19	4×10^{-25}	15,000
Natrolite	25	6×10^{-25}	10,000
Antigorite	12	5×10^{-25}	10,000
Lizardite	−15	1×10^{-25}	50,000
Labradorite	36	1×10^{-24}	6000
Apatite	6	2×10^{-25}	30,000
Hematite	14	3×10^{-25}	20,000

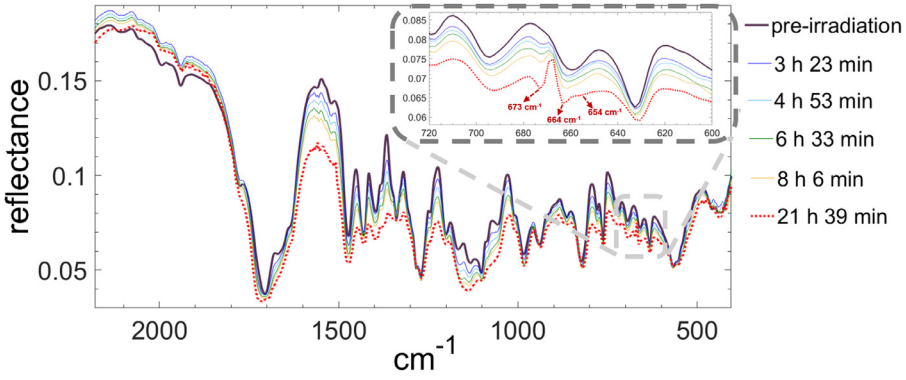

Fig. 10. Superposition of infrared spectra of pure UMP in the region 450–2200 cm^{-1} obtained over time during *in situ* UV irradiation under ambient conditions. The inset highlights the 600–720 cm^{-1} spectral region where the formation of a new peak at 673 cm^{-1} and the splitting of the peak at 661 cm^{-1} are observed. (For interpretation of the references to colour in this figure legend, the reader is referred to the web version of this article.)

After 40 hours of UV irradiation under simulated Martian conditions inside the PALLAS chamber, we observed slight degradation just for a few peaks of pure AMP corresponding to the C–H groups, at a much slower rate with respect to ambient conditions, without formation of any new peak (see Table 3 and Table 3s of ESI). Therefore, in the absence of minerals, we can infer that AMP is overall very stable because it undergoes only slight perturbation due to UV irradiation.

Also in the case of pure UMP, we observed decrease in intensity as effect of UV irradiation under Martian-like conditions only for a few infrared bands corresponding to C=C stretching of uracil moiety and C–H and O–H bending of ribose moiety, at a much slower rate than ambient conditions. For pure UMP we observed also changes in the 650–700 cm^{-1} spectral region that may be ascribed to formation of cyclobutane uracil dimers, consistently with previous experiments under terrestrial conditions, confirming that the uracil moiety is more photoreactive than the adenine one.

However, on average, the degradation cross-sections for AMP and UMP under Martian-like conditions turned out to be similar, *i.e.* 8×10^{-26} cm^2 and 2×10^{-25} cm^2, corresponding to half-lifetimes of about 70,000 and 40,000 Martian days, respectively.

The greater photostability demonstrated by the nucleotides AMP and UMP under Martian-like conditions with respect to ambient terrestrial conditions can be easily explained considering that we performed UV processing in totally absence of atmospheric oxygen after evacuation of air from the PALLAS chamber, then filled with a 6 mbar carbon dioxide atmosphere. Carbon dioxide has also proved to act as scavenger of free radicals (Vesela and Wilhelm, 2002). The less oxidative conditions inside the PALLAS chamber would prevent formation of very reactive radicals that may promote decomposition of nucleotides.

Furthermore, the lower temperature inside the chamber may be responsible for slowing down the degradation kinetics. These results suggest that current Martian conditions - 6 mbar carbon dioxide atmosphere and average temperature below 0 °C - favor better preservation of important “building blocks of life” such as nucleotides subjected to UV irradiation.

4.2.2. Degradation under ambient terrestrial conditions of nucleotides adsorbed on lizardite through equilibrium adsorption

Under ambient terrestrial conditions, we performed preliminary *in situ* UV irradiation experiments of AMP and UMP adsorbed on lizardite at equilibrium. With our interferometer we were able to clearly detect and analyse just one peak at 1600 cm^{-1} attributable to AMP adsorbed on lizardite. We compared the degradation rate of this peak with respect to the analogous peak for pure AMP. Under ambient conditions, we observed similar degradation kinetics, as reported in Table 2 and shown in Fig. 11, indicating that lizardite does not behave as a catalyst. However, as shown in Fig. 12, under

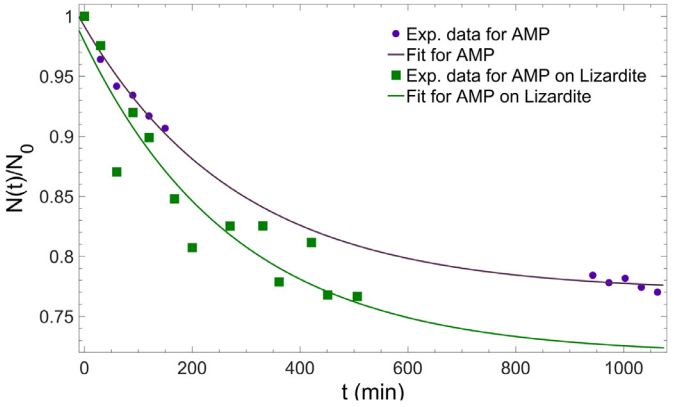

Fig. 11. Fits of degradation curves obtained through *in situ* UV irradiation experiments under ambient conditions for the AMP peak around 1600 cm^{-1} in the case of the pure AMP (violet circles) and AMP adsorbed on lizardite (green squares). Fit model: $N(t)/N_0 = Be^{-\beta t} + C$. For pure AMP: $B = 0.221 \pm 0.005$, $\beta = 0.0035 \pm 0.0004$ min^{-1}, $C = 0.771 \pm 0.005$, $R^2 = 0.9965$. For AMP adsorbed on lizardite: $B = 0.26 \pm 0.03$, $\beta = 0.004 \pm 0.001$ min^{-1}, $C = 0.72 \pm 0.03$, $R^2 = 0.8839$. (For interpretation of the references to colour in this figure legend, the reader is referred to the web version of this article.)

ambient conditions lizardite appears to promote the formation of a new peak at 2164 cm^{-1}.

For UMP adsorbed on lizardite, unfortunately, it was not possible to analyse the degradation kinetics under ambient conditions because we were not able to detect any peak of the molecule for this sample with our interferometer. Moreover, we did not notice any new peak indicative of the formation of cis-syn cyclobutane uracil dimers, but we observed a new peak at 2164 cm^{-1} as in the case of AMP adsorbed on lizardite.

As reported in Table 2, for both AMP and UMP adsorbed on lizardite, we estimated a formation cross-section for the new species appearing at 2164 cm^{-1} of the order of 10^{-22} cm^2. Such a spectroscopic feature is definitely not due to the formation of a cis-syn cyclobutane dimer because the infrared spectrum of the cyclobutane dimer does not present any band between 2000 and 2800 cm^{-1} (Varghese, 1971). Instead, it may be plausibly attributed to a cyanate molecular fragment OCN^-, which is well-known in the literature (Hudson et al., 2001; Schutte and Greenberg, 1997) for the 4.62-micron absorption feature in grain mantles of protostellar objects like W33A (Grim and Greenberg, 1987) and RAFGL 7009S (Demyk et al., 1998). Several studies show the formation of the cyanate fragment from a variety of decomposition pathways of nucleobases by vacuum UV radiation (Jochims et al., 2005), low- and high-energy electrons (Abdoul-Carime et al., 2005; Denifl et al., 2004; Evans et al., 2011; Góbi et al., 2017), and UVC (Ryszka et al., 2016). Feil et al. (2004) determined a cross-section for cyanate formation following electron impact on uracil that is of the same order of the one determined in this work for the new species formed during UV irradiation of AMP and UMP adsorbed on lizardite under terrestrial atmospheric conditions.

It is important to note that this spectroscopic feature around 2160 cm^{-1} emerges only when two conditions were met: 1) presence of the mineral surface, suggesting the attachment of such a new species to the surface sites; and 2) UV irradiation under terrestrial atmospheric conditions, while previous experiments performed in vacuum (Fornaro et al., 2013b) and the experiments carried out in this work under carbon dioxide atmosphere did not show the appearance of this band. In order to get insights into the formation mechanism of such species, we also performed UV irradiation under terrestrial atmospheric conditions of untreated lizardite and other minerals like brucite (data not shown). Overall, the mineral peaks did not change during UV irradiation, but we observed the formation of the same species around 2160 cm^{-1}, maybe due to the presence of nitrogen-bearing organic contaminations in the mineral samples that generate the cyanate fragment

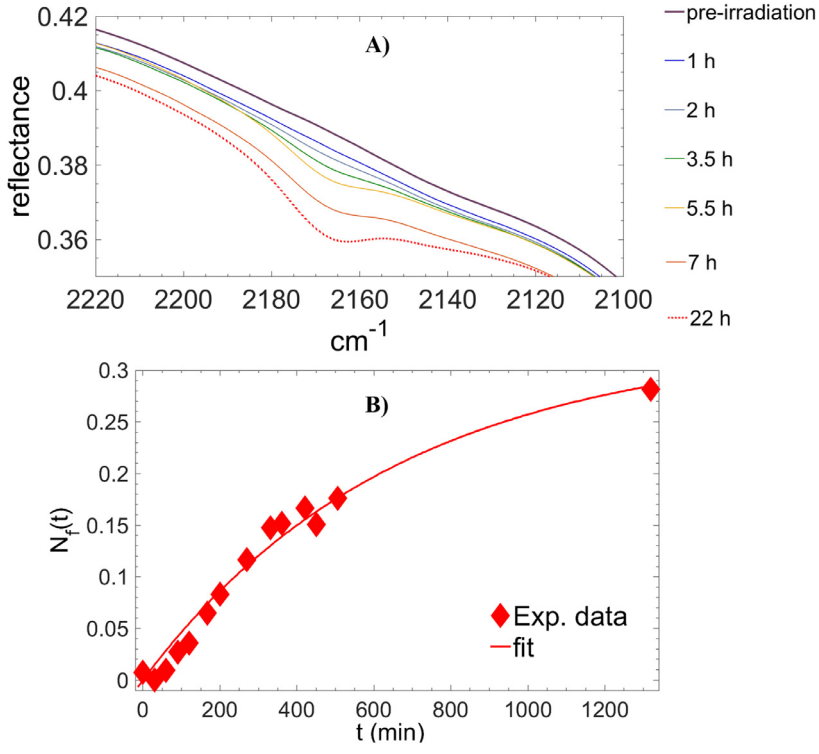

Fig. 12. Formation of a new peak at 2164 cm^{-1} during UV irradiation under ambient conditions of AMP adsorbed on lizardite. **A)** Superposition of infrared spectra of AMP adsorbed on lizardite in the region 2100–2220 cm^{-1} obtained over time. **B)** Fit model for formation of the peak at 2164 cm^{-1}: $N_f(t) = N_{f0} \cdot (1\text{-}e^{-\alpha t})$; $N_{f0} = 0.33 \pm 0.03$, $\alpha = 0.0015 \pm 0.0002$ min^{-1}, $R^2 = 0.9743$. (For interpretation of the references to colour in this figure legend, the reader is referred to the web version of this article.)

upon UV irradiation in air. Therefore, the cyanate fragments appear to be very common species generally formed in the presence of atmospheric oxygen. From such experimental outcomes, we can deduce that the formation mechanism likely involves surface functional groups like hydroxyls, which represent a common feature of hydroxylated minerals like lizardite and brucite, and reactive oxygen radicals produced by UV-photolysis of molecular atmospheric oxygen. However, further investigations are required to better understand the formation of the cyanate fragment under terrestrial atmospheric conditions.

Of note, Poch et al. (2015, 2014) performed similar UV irradiation experiments of pure adenine and adenine adsorbed on nontronite, observing the appearance of a sharp new peak at 2165–2180 cm^{-1} also under simulated Martian conditions, both for the pure molecule and adsorbed on the mineral, plus broad absorptions in the 3600–3000 cm^{-1} and 1800–1300 cm^{-1} spectral ranges. They interpreted the results as the formation of photoproducts bearing primary amine functional groups ($-NH_2$), isocyanides ($R-N{\equiv}C$) and/or nitriles ($R-C{\equiv}N$) involved in an extended conjugated system (as $-C=C-C=N-$). The increase of absorbance between 190 and 300 nm observed by Poch et al. (2014) upon UV irradiation of adenine, along with the change of colour of the adenine powder from white to slight yellow (observed also in our experiment), can indicate such extended conjugated systems. Poch et al. (2014) excluded the formation of cyanate ion in their UV irradiation experiments of adenine due to the absence of possible oxygen sources in their experimental conditions. However, in our experiments in terrestrial atmosphere, molecular oxygen may dissociate in the presence of UV radiation, opening new possible photochemical pathways for the adenine moiety, like the one described by Góbi et al. (2017) in which an active oxygen atom originating from radiolysis of magnesium perchlorate attacks the carbon atom at position 2 of adenine, yielding 2-oxo adenine (or isoguanine) that may evolve toward the formation of isocyanate (OCN^-).

4.2.3. Degradation under ambient Martian-like conditions of nucleotides adsorbed on minerals through equilibrium adsorption

In the next set of experiments, we performed *ex situ* UV irradiation under Martian-like conditions inside the PALLAS chamber of AMP and UMP adsorbed on the various minerals through equilibrium adsorption. The infrared spectra of nucleotides adsorbed on the different minerals before and after UV irradiation under Martian-like conditions inside the PALLAS chamber are reported in Fig. 7s and 8s of ESI.

For AMP adsorbed on lizardite, the infrared spectra before and after UV irradiation under Martian-like conditions are shown in Fig. 13. Also in this case, under Martian-like conditions, a slower degradation with respect to ambient conditions occurred for the same peak at 1600 cm^{-1} for AMP adsorbed on lizardite. Specifically, we determined a cross-section of the order of 10^{-25} cm^2 and a half-lifetime of about 30,000 Martian days. The average cross-section for all detectable peaks was of the order of 10^{-25} cm^2 with a half-lifetime of about 40,000 Martian days as reported in Table 4. Very importantly, we did not observe formation of the new peak at 2164 cm^{-1}, confirming that the lower temperature and the carbon dioxide atmosphere stabilize the nucleotides.

For UMP adsorbed on lizardite, under Martian-like conditions we noticed no formation of the new peak at 2164 cm^{-1} and a slower degradation with respect to ambient conditions, with half-lifetimes of about 49,000 Martian days, confirming again a higher photostability of nucleotides in a Martian-like environment. Comparing the degradation kinetics of analogous peaks for UMP adsorbed on lizardite and pure UMP, it appears that lizardite is not able to catalyze any degradation (negative degrading power in Table 4). On the contrary, lizardite seems to slow down degradation with respect to the pure molecule, acting as protector against UV radiation. However, it is important to note that for such a sample we were able to detect only a few weak peaks of the molecule, and such low signal to noise ratio makes definite interpretation of the data more difficult.

Overall, the serpentine minerals lizardite and antigorite demonstrated negligible degrading power as shown in Table 4. Lizardite exhibited very slight degradation (about 10%) for the detectable peaks of AMP adsorbed on the mineral. We estimated the same degradation kinetics for antigorite with 12% of degradation corresponding to a half-lifetime of degradation of the order of 30,000 Martian days. Also in the case of UMP adsorbed on antigorite, we were able to detect only a few weak peaks of the molecule, whereby we determined a degrading power of about 12% with respect to pure UMP.

The analysis of degradation of the peaks for AMP adsorbed on forsterite, by contrast, indicated that the mineral catalyzes degradation of AMP with respect to pure AMP. Indeed, as reported in Table 3, among the 14 detectable peaks of AMP, 11 underwent degradation, with an average degradation percentage of about 29% in 40 hours of UV irradiation under Martian-like conditions. This value corresponds to a half-lifetime of about 10,000 Martian days, which is shorter than the analogous cases for lizardite and antigorite previously examined. Forsterite appeared to be photocatalytic also for degradation of UMP with respect to pure UMP. As reported in Table 3, among the 11 detectable peaks of UMP, 6 underwent degradation with an average degradation percentage of about 19% relative to the degradation of analogous peaks of pure UMP in 40 hours of UV irradiation inside the PALLAS chamber, which corresponds to a half-lifetime of about 15,000 Martian days.

In the case of AMP adsorbed on natrolite, we noticed a higher degrading power with an average degradation percentage of 75%, which corresponds to a half-lifetime of about 3000 Martian days. For UMP adsorbed on natrolite, as reported in Table 3, 5 of the 6 peaks detected underwent degradation and the estimated degrading power for natrolite was about 25% with respect to pure UMP, corresponding to a half-lifetime of about 10,000 Martian days.

Labradorite presented the greatest catalytic activity, as clearly shown by the decrease in the intensity of the infrared bands attributable to AMP in Fig. 14, giving 77% of degradation for AMP, which corresponds to a half-lifetime of about 3000 Martian days. We observed significant degradation for the peaks of UMP adsorbed on labradorite as well, with an estimated degrading power of about 36% with respect to pure UMP, corresponding to a half-lifetime of about 6000 Martian days.

Apatite did not show any catalytic effect for degradation of AMP, giving on average about 2% degradation. Also in the case of UMP, apatite exhibited very low degrading power (about 6%), corresponding to a half-lifetime of about 30,000 Martian days.

The degrading power estimated for hematite was intermediate, both for AMP (25% on average) and UMP (14% on average).

In summary, we estimated the following overall effects for AMP degradation: labradorite (77%) $\geq$ natrolite (75%) $>>$ forsterite (29%) $>$ hematite (25%) $>$ antigorite (12%) $\approx$ lizardite (10%) $>$ apatite (2%). As shown in Table 3, even though pure AMP shows high photostability, when AMP is adsorbed onto forsterite, natrolite and labradorite, most of the detectable infrared peaks of AMP underwent degradation, indicating that these minerals promote the degradation process. In the case of hematite, only specific infrared peaks of AMP were affected by UV irradiation. In the case of AMP adsorbed on the serpentine minerals, antigorite and lizardite, it appears that the ribose moiety is not involved in the degradation mechanism, because the few detected C–H stretching peaks were not perturbed by UV irradiation, but slight degradation of the adenine moiety occurred. In the case of AMP adsorbed on apatite, an

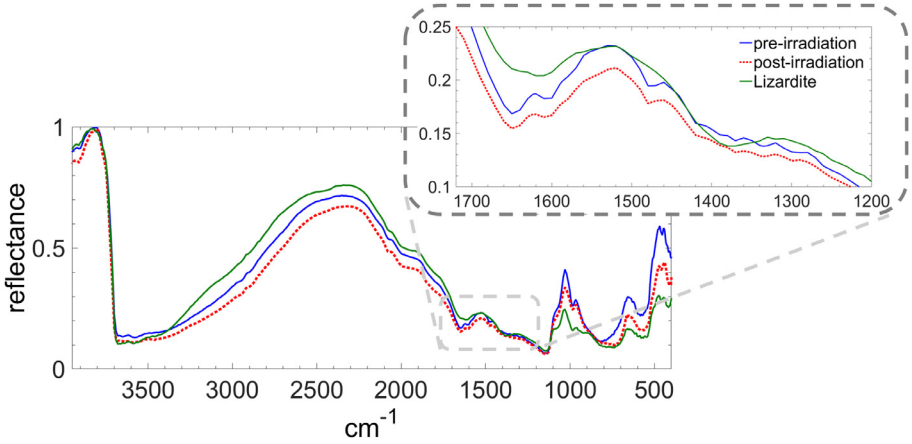

Fig. 13. Infrared spectra of AMP adsorbed on lizardite pre- and post- UV irradiation under Martian-like conditions inside the PALLAS chamber compared to the spectrum of untreated lizardite. The inset highlights the 1200–1700 cm^{-1} spectral region where the peaks of AMP are detected. (For interpretation of the references to colour in this figure legend, the reader is referred to the web version of this article.)

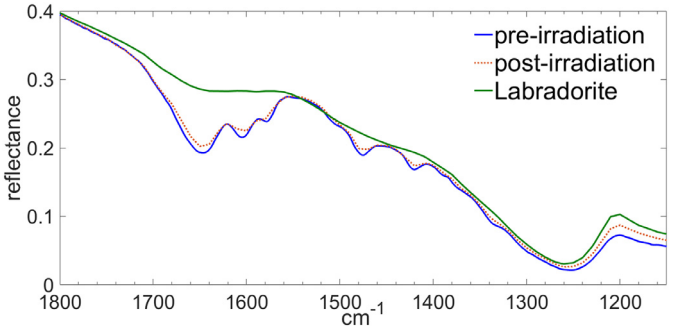

Fig. 14. Infrared spectra of AMP adsorbed on labradorite pre- and post- UV irradiation under Martian-like conditions inside the PALLAS chamber compared to the spectrum of untreated labradorite. (For interpretation of the references to colour in this figure legend, the reader is referred to the web version of this article.)

insignificant intensity decrease was observed just for few modes of the adenine moiety.

From degradation data of UMP samples, we estimated a similar degrading trend of these minerals: labradorite (36%) > natrolite (25%) > forsterite (19%) > hematite (14%) > antigorite (12%) > apatite (6%) > lizardite (−15%). Table 3 shows that the carbonyl group of the uracil moiety, whose stretching vibration is characterized by an intense peak in the infrared spectrum, was not perturbed both in the case of pure UMP and UMP adsorbed on the minerals, except for a slight decrease in intensity in the presence of lizardite. Instead, the ribose moiety seemed to be more affected by UV radiation. Overall, the trend in degrading UMP for the different minerals follows the one observed in the case of AMP, with apatite and serpentine minerals featuring more photoprotective properties.

4.2.4. Possible degradation mechanisms under ambient Martian-like conditions of nucleotides adsorbed on minerals through equilibrium adsorption

Unfortunately, we could not unravel the degradation pathways solely from observation of changes in the infrared spectra because we detected very few spectroscopic features ascribable to nucleotide molecules adsorbed on the minerals, without clear evidence of formation of photoproducts during UV irradiation. Therefore, further studies are required to get insights into the underlying photochemical mechanisms and explain the different catalytic behaviour of these minerals toward the degradation of nucleotides under simulated Martian conditions. However, it is possible to discuss the main trends emerging from the experimental outcomes, summarizing that, among the different minerals analyzed, labradorite and natrolite feature the greatest catalytic activity, hematite and forsterite have an intermediate behaviour, while apatite, lizardite and antigorite do not show any significant catalytic effect.

Our results are in agreement with recent UV irradiation studies of amino acids adsorbed on various minerals under Martian-like conditions carried out by dos Santos et al. (2016), showing an overall greater preservation potential in the case of clay phyllosilicate minerals, including nontronite, montmorillonite and saponite, with respect to iron oxides (*e.g.*, hematite) and feldspars (*e.g.*, labradorite). They argued that clay minerals preserve amino acids due to their high surface areas and, consequently, high number of sites available for surface interactions favoring molecular adsorption. In addition, the small pore sizes typical of clay minerals create a shielded environment by limiting penetration of radiation in the inner part of the mineral, and thus protect the adsorbed molecules from direct exposure to UV radiation.

Other studies specifically point out the photoprotective properties of phyllosilicates such as nontronite, montmorillonite and kaolinite for nucleic acid components (Biondi et al., 2007; Negron-Mendoza et al., 2010; Poch et al., 2015; Scappini et al., 2004). Evidence suggests that such a photoprotective effect is not only due to mechanical shielding provided by mineral grains, but a sort of stabilizing physico-chemical interactions between molecules and mineral surface (not yet clarified) should be involved as well (Poch et al., 2015). The photoprotective properties/low catalytic activity observed for the serpentine minerals analysed in this work, lizardite and antigorite, confirm that phyllosilicates are capable of protecting nucleic acid components from damaging effects of UV radiation.

In the case of minerals containing transition metals like iron, the catalytic/protective properties depend on a subtle balance between multiple phenomena (dos Santos et al. (2016), and references therein). On the one hand, transition metals possess UV-photoprotective properties due to the presence of *d* orbitals, which facilitate much greater UV absorption. Consequently, higher photoprotection is expected with higher content of transition metals in the mineral (Hoang-Minh et al., 2010). We noticed a similar correlation for the serpentine minerals, whose XRF analyses show a significant iron content (Table 1). On the other hand, transition metals and their compounds may act as catalysts because they have partially filled *d* sub-shells and they easily give and take electrons from other molecules, adopting multiple oxidation states and forming complexes (Bersuker, 2010). For example, in our current

experiments of UV irradiation of nucleotides and previous irradiation of nucleobases (Fornaro et al., 2013b), the catalytic activity of forsterite may reflect the relatively high content of iron measured through XRF (Table 1). Transition metal oxides like hematite feature small gaps between the valence and the conduction bands, so they can act as semiconductors. Specifically, electrons in the valence band can be easily excited to the conduction band by absorbing radiation, leaving an electron hole in the valence band and creating electron-hole pairs called excitons. These excitons have high mobility inside the mineral grains and may reach adsorbed molecules promoting redox reactions. In the presence of molecular oxygen or water molecules, excitons may lead to production of reactive oxygen species like superoxide radical anions, hydroxyl radicals and hydrogen peroxide radicals, which in turn may degrade adsorbed organic molecules. In the case of minerals with high iron content, water adsorbed at the surface of a mineral can leach soluble species from the rock, leading to favorable conditions for Fenton and photo-Fenton reactions that may contribute to molecular degradation (Benner et al., 2000). These processes may explain the catalytic activity observed in this work in the case of hematite for nucleic acid components and by dos Santos et al. (2016) for amino acids.

Zeolites like natrolite are known to be good adsorbents of organic compounds and have been used as photocatalysts to degrade different organic pollutants (Emdadi et al., 2017; Sadjadi and Heravi, 2017; Zhao et al., 2014). The degradation mechanism may involve separation of electron-hole pairs on the surface of zeolite under UV irradiation, which in the presence of molecular oxygen or water molecules (that are included into the structure of this mineral) may produce reactive radicals capable of degrading adsorbed organic molecules (Nassar and Abdelrahman, 2017).

A similar photodegradation process may explain the high catalytic activity of labradorite toward degradation of nucleotides observed in our experiments, in agreement with previous studies of degradation of organic compounds like amino acids (dos Santos et al., 2016) and phenols (Borges et al., 2008). These catalytic properties may be partly related to the presence of TiO_2 (even though its content is very low). TiO_2 may act either as photostabilizer or photocatalyst (Allen et al., 2004, 1998; Chen et al., 2007; Zeynalov and Allen, 2006). Photoprotection is due to its high UV absorption and good reflective properties. However, absorption of UV radiation by TiO_2 may cause photoionisation with formation of electron-holes pairs, which in turn may generate radicals in the presence of atmospheric oxygen and water (Hoffmann et al., 1995; Riegel and Bolton, 1995). Indeed, even though experiments were conducted inside the Martian simulation chamber in absence of atmospheric oxygen, water molecules chemisorbed on the surface of the mineral were certainly present. We verified that high vacuum is not sufficient to desorb the water molecules chemisorbed on the mineral surface by itself. However, we observed in some minerals the disappearance of the broad band of water around 3000 cm^{-1} by raising the temperature above 700 K. Therefore, under the conditions we used in our experiments inside the Martian simulation chamber, we cannot exclude the presence of water molecules that can be sources of radical species as consequence of UV irradiation. Yen et al. (2000) studied feldspars demonstrating that superoxide radicals are formed through the combination of cold mineral surfaces (−30 °C), Mars-like UV lighting, free oxygen, and low concentrations of water. Möhlmann (2004, 2008) theoretically predicted the ubiquitous presence of a few monolayers of water on exposed Martian surfaces. Therefore, degradation mechanisms driven by hydroxyl radicals can be considered plausible on Mars.

Regarding apatite, indications of possible photoprotective capabilities can be found in: 1) its proven low photocatalytic activity (Holzmann et al., 2009); 2) the UV luminescence of natural materials such as bone and teeth as well as modified apatite samples doped with certain metal cations (Blasse and Grabmaier, 1994; de Araujo et al., 2010), which provides an efficient mechanism for dissipation of excitation energy; and 3) its rather low refractive index (1.63–1.64) which may be responsible for reducing undesired light-scattering effects in the presence of organic matter.

Even though pure calcium halophosphates do not contain in general any noticeable inorganic chromophores and absorb only at very short wavelengths around 150 nm (Blasse and Grabmaier, 1994), XRF measurements of our apatite sample show the presence of manganese, chromium, titanium, cobalt and nickel impurities (see Table 1) that can replace calcium ion positions within the crystal lattice and modify the photophysical properties of this mineral, making it a better UV-absorber able to efficiently dissipate the excitation energy by several radiative pathways (Holzmann et al., 2009). Therefore, it is plausible that radiative deactivation pathways of UV-light excited states also take place in our apatite sample favoring preservation of adsorbed organic matter from destructive photoinduced degradation processes.

In summary, multiple factors are responsible for the overall behaviour of the different minerals under UV irradiation and the degradation mechanisms of adsorbed organic molecules may be the result of many simultaneous processes. For instance, the absorption of UV radiation may generate electron-hole pairs inside the mineral, followed by redox processes of the adsorbate due to electron transfers between molecules and the solid. In addition, molecular photolysis may be enhanced by adsorption onto a mineral surface because the interactions of a molecule with a mineral can weaken intramolecular bonds, facilitating their breakage. Furthermore, iron (II)-catalyzed reactions in the presence of reactive oxygen species (Fenton and photo-Fenton processes) may occur with iron-bearing minerals. By contrast, other minerals possess structural properties or electronic and optical features (*e.g.*, opacity to UV radiation, UV luminescence, low refractive index) that confer shielding effects for adsorbed molecules. All these different processes must be taken into account to explain the photostability of the adsorbed organic molecules.

4.2.5. Degradation of nucleotides adsorbed on minerals through incipient wetness impregnation

We report no data for samples prepared by water deposition, because unfortunately the results obtained from UV irradiation experiments were not reliable. This problem is likely related to the high concentration of nucleotide molecules, which leads to behaviours that are difficult to interpret due to intermolecular interactions. Hence, the preparation method of the Mars soil analogues seems to influence the photodegradation processes. dos Santos et al. (2016) pointed out that minerals display a different degrading power depending on the concentration of amino acids spiked on the minerals, observing in general a higher preservation with increasing molecular concentration, maybe due to the occupation of less exposed sites and shielding effects related to intermolecular association.

We noticed the same trend in our experiments, by preparing equilibrium samples containing 5% of nucleotides and spiked samples containing 10% of nucleotides. In the case of spiked samples at higher organic concentration, we were not able to obtain any useful information about mineral properties likely due to strong intermolecular associations, which may favorably take place through strong hydrogen bonding networks among nucleotide molecules. The formation of such molecular clusters, whose behaviour is similar to the pure nucleotides, hides the real effect of the surface on the molecules directly interacting at the interface. These observations indicate that sample preparation methods based on equilibrium adsorption processes are more likely to provide direct access to surface properties. With the typical sample preparation methods by water deposition, it is possible to adsorb a specific quan-

tity of molecules on the solid support, but there is no control of pH and coverage, and it is not possible to investigate the physicochemical interactions established during an equilibrium process between mineral substrate and molecules in aqueous phase, because molecules likely adsorb in a random way. Instead, the equilibrium adsorption method facilitates studies of the specific intermolecular interactions, controlling experimental conditions and degree of coverage. Actually, in this specific study, we cannot rule out the existence of intermolecular interactions also in the case of equilibrium samples due to their high organic content. However, the equilibrium adsorption procedure maximizes the interactions between mineral surface and molecules as well as possible molecular diffusion inside the mineral matrix, allowing overall a better study of the effects of mineral matrices on adsorbed organic molecules.

The two preparation methods also simulate the formation of molecule-mineral complexes in different environments. In particular, the water deposition method mimics superficial phenomena like evaporation of warm little ponds of liquid water / desiccation of liquid water bodies, whereas the equilibrium adsorption better simulates natural adsorption processes occurred over long periods of time in dilute surface/subsurface aqueous environments like those presumably present on Noachian Mars.

4.3. Implications for space missions to Mars

Laboratory simulations of the Martian environment are essential to support both *in situ* exploration and sample return space missions devoted to detection of molecular biomarkers on Mars. Indeed, they may provide important information about the processing experienced by potential biomarkers under harsh Martian conditions, which helps in the evaluation of conditions suitable for the preservation of signs of past or present life on Mars, to correctly interpret data collected on the ground and to develop suitable life detection methods and technologies for analyses both on the ground and in terrestrial laboratories.

UV radiation and perchlorates are among the main degradation agents on Mars (Benner et al., 2000; Hassler et al., 2014; Kounaves et al., 2014), whose effect on the stability and reactivity of possible biomarkers embedded in the Martian soil strongly depends on the protective or catalytic properties of the mineral matrices (Brucato and Fornaro, 2018; dos Santos et al., 2016). A systematic study of the effects of UV radiation and the presence of perchlorates on a variety of possible Mars soil analogues is key to figure out which mineral deposits are more suitable to preserve potential biomarkers on Mars and for developing models for their degradation at geological time-scales. This information would be particularly helpful to select the future landing sites on Mars for collecting samples to return to Earth.

Moreover, the characterization of Mars soil analogues through various non-destructive techniques allows us to assay the sensitivity of different laboratory instruments to detect diagnostic features of molecular biomarkers (Fornaro et al., 2018; Steele et al., 2012) and, hence, supports the technology development of flight instruments.

Accordingly, this work explores the potentialities of different techniques, such as ToF-SIMS, Infrared and Raman vibrational spectroscopies, to detect diagnostic features of important molecular biomarkers of extant life like nucleotides adsorbed on different mineral matrices, highlighting their complementarity, which can be crucial for the interpretation of data collected on the ground during mission operative periods. These studies are particularly valuable for future space missions like *ExoMars 2020* and *Mars 2020*, in which Infrared and Raman spectrometers, namely *MicrOmega* (Leroi et al., 2009; Pilorget et al., 2012), *Raman Laser Spectrometer* (*RLS*) (Edwards et al., 2012), and *Scanning Habitable Environments with Raman and Luminescence for Organics and Chemicals* (*SHERLOC*) (Abbey et al., 2017; Beegle and Bhartia, 2016), will be used not only for the study of Martian mineralogy but also to look for possible molecular biomarkers in the Martian soil. About ToF-SIMS, it has been demonstrated that this ion probe technique is capable of detecting and identifying several organic compounds, including poly- and heterocyclic aromatic hydrocarbons, and it can augment GC–MS analysis on small geological samples (Siljeström et al., 2009; Toporski and Steele, 2004). Moreover, ToF-SIMS is similar to the Laser Desorption Ionization Mass Spectrometry (LDI-MS) technique, which will be used for detecting organic compounds by the *Mars Organics Molecule Analyser* (*MOMA*) instrument (Goetz et al., 2016) on board the *ExoMars* rover. Specifically, ToF-SIMS uses ions instead of a laser to create ions to analyse in the mass spectrometer. Despite the difference, ToF-SIMS produces very similar peaks with respect to LDI, and it can be used to understand ion generation in LDI (private communication, Sandra Siljeström).

Moreover, the results obtained from the UV irradiation experiments allowed us to compare the photoprotective/photocatalytic behaviour of a variety of minerals relevant to Mars mineralogy and make predictions for the mineral deposits that have the highest preservation potential on Mars.

Specifically, among the minerals providing greater protective properties, apatite draws particular attention because its distribution on Mars may help in tracing habitability, since this mineral is considered a plausible geological source of phosphorus, an essential element for life on Earth, and it has been argued that phosphate minerals might have been involved in crucial prebiotic processes (Costanzo et al., 2007).

Lizardite and antigorite are phyllosilicates of the serpentine subgroup of great interest for both prebiotic chemistry and their presence on Mars. The capability of these minerals to protect important “building blocks of life” such as nucleotides against damaging UV radiations is encouraging for detecting biomarkers on Mars. Indeed, the primary candidates as landing sites for future exploration missions on Mars devoted to life detection are characterized by the presence of phyllosilicate minerals, which are indications of aqueous alterations that occurred in Mars history.

In agreement with previous findings by dos Santos et al. (2016), our data prove that olivine, feldspars, zeolites and iron oxides do not facilitate preservation of important molecular biomarkers of extant life such as amino acids and nucleotides. Especially feldspars and zeolites should not be targeted for the detection of biomarkers in future life detection missions to Mars because they strongly promote degradation of the biomarkers in the presence of UV radiation.

5. Conclusions

The main activities performed in this work consist of: 1) preparation of Mars soil analogues, by doping natural and synthetic minerals with organic compounds considered as potential biomarkers; 2) characterization of Mars soil analogues by means ToF-SIMS, infrared and Raman vibrational spectroscopies; and 3) UV irradiation processing of biomarkers adsorbed on minerals under Martian-like conditions.

Specifically, we focused on several minerals that are abundant on Mars and are interesting for prebiotic processes, namely the serpentines lizardite and antigorite, the plagioclase feldspar labradorite, the zeolite natrolite, the iron oxide hematite, the olivine forsterite, and the phosphate apatite.

Regarding astrobiologically relevant molecules, we considered nucleic acid components such as adenosine monophosphate (AMP) and uridine monophosphate (UMP), which are biomarkers of extant life particularly important also in the prebiotic context.

Sample preparation based on the equilibrium adsorption method turned out to be the best for studying the effects of the mineral surfaces on the molecules directly interacting with the surface sites.

Infrared spectroscopy, micro-Raman imaging, and ToF-SIMS techniques proved to be highly complementary for detecting the diagnostic features of nucleotides adsorbed on minerals, which is particularly valuable for the interpretation of scientific data that will be collected during *in situ* exploration of Mars by space missions like *ExoMars 2020* and *Mars 2020*.

We used the Mars soil analogues prepared and characterized in the laboratory to simulate the UV processing occurring on Mars within a Martian simulation chamber by recreating the typical conditions of Martian environment of 6 mbar carbon dioxide atmosphere, temperatures below 0 °C, and UV irradiation most significant in the mid-UV spectral region. In order to study the effects of UV irradiation on Mars soil analogues, we recorded infrared spectra of the samples before and after UV processing. For comparison, we carried out analogous experiments under terrestrial ambient conditions using a different experimental setup, which allows *in situ* UV irradiation, *i.e.* infrared spectroscopic analysis takes place during UV irradiation without moving the sample. We observed in general that degradation under Martian-like conditions occurs much slower than in terrestrial ambient conditions, indicating that current Martian conditions favor preservation of potential biomarkers embedded in Mars analogue mineral matrices.

The results of UV irradiation experiments under simulated Martian conditions indicate that, among the different minerals analyzed, labradorite and natrolite possess significant catalytic abilities, hematite and forsterite have an intermediate degrading effect, while apatite, lizardite and antigorite do not promote any significant degradation of nucleotides.

These experimental outcomes are particularly helpful for supporting the choice of the landing site for future space missions to Mars. Such laboratory investigations are useful also during mission operative periods for selecting the most interesting drilled Martian samples to be analyzed in more detail after a pre-screening of their composition and mineralogy. Moreover, the study of photodegradation of potential biomarkers under Martian-like conditions is critical for a correct interpretation of the data collected on the ground, and for identification of biomarkers that are more likely to be detected in a Martian environment.

Acknowledgements

The authors acknowledge Helen King of the Utrecht University, Dionysis Foustoukos and Timothy Strobel of the Carnegie Institution for Science, for their scientific and technical assistance throughout this work. This research was supported by the COST Action TD1308-Origins, the NASA grant NNX13AJ19G (A. Steele PI), the Swedish National Space Board (contract 198/15), the Italian Space Agency (ASI) grant agreement ASI/INAF n. 2015-002-R.0.

Supplementary materials

Supplementary material associated with this article can be found, in the online version, at doi:10.1016/j.icarus.2018.05.001.

References

Abbey, W.J., Bhartia, R., Beegle, L.W., DeFlores, L., Paez, V., Sijapati, K., Sijapati, S., Williford, K., Tuite, M., Hug, W., Reid, R., 2017. Deep UV Raman spectroscopy for planetary exploration: the search for *in situ* organics. Icarus 290, 201–214.

Abdoul-Carime, H., Langer, J., Huels, M.A., Illenberger, E., 2005. Decomposition of purine nucleobases by very low energy electrons. Eur. Phys. J. D 35, 399–404.

Allen, N.S., Edge, M., Corrales, T., Catalina, F., 1998. Stabiliser interactions in the thermal and photooxidation of titanium dioxide pigmented polypropylene films. Polym. Degrad. Stab. 61, 139–149.

Allen, N.S., Edge, M., Ortega, A., Sandoval, G., Liauw, C.M., Verran, J., Stratton, J., McIntyre, R.B., 2004. Degradation and stabilisation of polymers and coatings: nano *versus* pigmentary titania particles. Polym. Degrad. Stab. 85, 927–946.

Arvidson, R.E., Poulet, F., Morris, R.V., Bibring, J.-P., Bell, J.F., Squyres, S.W., Christensen, P.R., Bellucci, G., Gondet, B., Ehlmann, B.L., Farrand, W.H., Fergason, R.L., Golombek, M., Griffes, J.L., Grotzinger, J., Guinness, E.A., Herkenhoff, K.E., Johnson, J.R., Klingelhöfer, G., Langevin, Y., Ming, D., Seelos, K., Sullivan, R.J., Ward, J.G., Wiseman, S.M., Wolff, M., 2006. Nature and origin of the hematite-bearing plains of Terra Meridiani based on analyses of orbital and Mars Exploration rover data sets. J. Geophys. Res. Planets 111.

Atreya, S.K., Mahaffy, P.R., Wong, A.-S., 2007. Methane and related trace species on Mars: origin, loss, implications for life, and habitability. Planet. Space Sci. 55, 358–369.

Bach, W., Paulick, H., Garrido, C.J., Ildefonse, B., Meurer, W.P., Humphris, S.E., 2006. Unraveling the sequence of serpentinization reactions: petrography, mineral chemistry, and petrophysics of serpentinites from MAR 15 N (ODP Leg 209, Site 1274). Geophys. Res. Lett. 33.

Banin, A., Lawless, J.G., Mazzurco, J., Church, F.M., Margulies, L., Orenberg, J.B., 1985. pH profile of the adsorption of nucleotides onto montmorillonite. Orig. Life Evol. Biosph. 15, 89–101.

Barbatti, M., Aquino, A.J.A., Szymczak, J.J., Nachtigallová, D., Hobza, P., Lischka, H., 2010. Relaxation mechanisms of UV-photoexcited DNA and RNA nucleobases. Proc. Natl. Acad. Sci. 107, 21453–21458.

Beegle, L., Bhartia, R., 2016. SHERLOC: an investigation for Mars 2020. Geophys. Res. Abstr. EGU Gen. Assem. 18 EGU2016-11215.

Bell, J.F., McSween, H.Y., Crisp, J.A., Morris, R.V., Murchie, S.L., Bridges, N.T., Johnson, J.R., Britt, D.T., Golombek, M.P., Moore, H.J., Ghosh, A., Bishop, J.L., Anderson, R.C., Brückner, J., Economou, T., Greenwood, J.P., Gunnlaugsson, H.P., Hargraves, R.M., Hviid, S., Knudsen, J.M., Madsen, M.B., Reid, R., Rieder, R., Soderblom, L., 2000. Mineralogic and compositional properties of Martian soil and dust: results from Mars Pathfinder. J. Geophys. Res. Planets 105, 1721–1755.

Benner, S.a, Devine, K.G., Matveeva, L.N., Powell, D.H., 2000. The missing organic molecules on Mars. Proc. Natl. Acad. Sci. U. S. A. 97, 2425–2430.

Bersuker, I.B., 2010. Electronic Structure and Properties of Transition Metal Compounds: Introduction to the Theory. John Wiley & Sons, Inc, Hoboken, NJ, USA.

Bibring, J.-P., Langevin, Y., Gendrin, A., Gondet, B., Poulet, F., Berthé, M., Soufflot, A., Arvidson, R., Mangold, N., Mustard, J., Drossart, P., Team, O., 2005. Mars surface diversity as revealed by the OMEGA/Mars Express observations. Science 307, 1576–1581.

Bibring, J.P., Langevin, Y., Mustard, J., 2006. Global mineralogical and aqueous Mars history derived from OMEGA/Mars Express data. Science 312, 400–404.

Biemann, K., 1979. The implications and limitations of the findings of the Viking organic analysis experiment. J. Mol. Evol. 14, 65–70.

Biondi, E., Branciamore, S., Maurel, M.-C., Gallori, E., 2007. Montmorillonite protection of an UV-irradiated hairpin ribozyme: evolution of the RNA world in a mineral environment. BMC Evol. Biol. 7, S2.

Biondi, E., Howell, L., Benner, S.A., 2016. Opal absorbs and stabilizes RNA – a hierarchy of prebiotic silica minerals. Synlett 27 A-E.

Blasse, G., Grabmaier, B.C., 1994. Energy transfer. In: Luminescent Materials. Springer Berlin Heidelberg, Berlin, Heidelberg, pp. 91–107.

Borges, M.E., Alvarez-Galván, M.C., Esparza, P., Medina, E., Martín-Zarza, P., Fierro, J.L.G., 2008. Ti-containing volcanic ash as photocatalyst for degradation of phenol. Energy Environ. Sci. 1, 364–369.

Brucato, J.B., Fornaro, T., 2018. Role of mineral surfaces in prebiotic processes and space-like conditions. In: Cavalazzi, B., Westall, F. (Eds.), Biosignatures for Astrobiology. Springer Int. Pub. p. In press.

Brucato, J.R., Strazzulla, G., Baratta, G.A., Rotundi, A., Colangeli, L., 2006. Cryogenic synthesis of molecules of astrobiological interest: catalytic role of cosmic dust analogues.. Orig. Life Evol. Biosph. 36, 451–457.

Burton, F.G., Neuman, M.W., Neuman, W.F., 1969. On the possible role of crystals in the origins of life. I. The adsorption of nucleosides, nucleotides and pyrophosphate by apatite crystals. Biosystems 3, 20–26.

Cairns-Smith, A.G., Hartman, H., 1986. Clay Minerals and the Origin of Life. Cambridge University Press.

Catling, D.C., Moore, J.M., 2003. The nature of coarse-grained crystalline hematite and its implications for the early environment of Mars. Icarus 165, 277–300.

Chen, X.D., Wang, Z., Liao, Z.F., Mai, Y.L., Zhang, M.Q., 2007. Roles of anatase and rutile TiO2 nanoparticles in photooxidation of polyurethane. Polym. Test. 26, 202–208.

Chevrier, V., Mathé, P.E., 2007. Mineralogy and evolution of the surface of Mars: a review. Planet. Space Sci. 55, 289–314.

Christensen, P.R., Bandfield, J.L., Clark, R.N., Edgett, K.S., Hamilton, V.E., Hoefen, T., Kieffer, H.H., Kuzmin, R.O., Lane, M.D., Malin, M.C., Morris, R.V., Pearl, J.C., Pearson, R., Roush, T.L., Ruff, S.W., Smith, M.D., 2000. Detection of crystalline hematite mineralization on Mars by the thermal emission spectrometer: evidence for near-surface water. J. Geophys. Res. Planets 105, 9623–9642.

Christensen, P.R., Morris, R.V., Lane, M.D., Bandfield, J.L., Malin, M.C., 2001. Global mapping of Martian hematite mineral deposits: remnants of water-driven processes on early Mars. J. Geophys. Res. Planets 106, 23873–23885.

Clifford, S.M., Lasue, J., Heggy, E., Boisson, J., McGovern, P., Max, M.D., 2010. Depth of the Martian cryosphere: revised estimates and implications for the existence and detection of subpermafrost groundwater. J. Geophys. Res. 115, E07001.

Cockell, C.S., 1998. Biological effects of high ultraviolet radiation on early earth-a theoretical evaluation. J. Theor. Biol. 193, 717–729.

Cockell, C.S., Catling, D.C., Davis, W.L., Snook, K., Kepner, R.L., Lee, P., Mckay, C.P., 2000. The ultraviolet environment of Mars: biological implications past, present, and future. Icarus 146, 343–359.
Costanzo, G., Saladino, R., Crestini, C., Ciciriello, F., Di Mauro, E., 2007. Nucleoside phosphorylation by phosphate minerals. J. Biol. Chem. 282, 16729–16735.
Crismani, M.M.J., Schneider, N.M., Plane, J.M.C., Evans, J.S., Jain, S.K., Chaffin, M.S., Carrillo-Sanchez, J.D., Deighan, J.I., Yelle, R.V., Stewart, A.I.F., McClintock, W., Clarke, J., Holsclaw, G.M., Stiepen, A., Montmessin, F., Jakosky, B.M., 2017. Detection of a persistent meteoric metal layer in the Martian atmosphere. Nat. Geosci. 10, 401–404.
Dartnell, L.R., Desorgher, L., Ward, J.M., Coates, A.J., 2007. Modelling the surface and subsurface Martian radiation environment: implications for astrobiology. Geophys. Res. Lett. 34, L02207.
de Araujo, T.S., de Souza, S.O., de Sousa, E.M.B., 2010. Effect of Zn^{2+}, Fe^{3+} and Cr^{3+} addition to hydroxyapatite for its application as an active constituent of sunscreens. J. Phys. Conf. Ser. 249, 12012.
Demyk, K., Dartois, E., D'Hendecourt, L., Jourdain de Muizon, M., Heras, a.M., Breitfellner, M., 1998. Laboratory identification of the 4.62 μm solid state absorption band in the ISO-SWS spectrum of RAFGL 7009S. Astron. Astrophys. 339, 553–560.
Denifl, S., Ptasińska, S., Hanel, G., Gstir, B., Probst, M., Scheier, P., Märk, T.D., 2004. Electron attachment to gas-phase uracil. J. Chem. Phys. 120, 6557–6565.
dos Santos, R., Patel, M., Cuadros, J., Martins, Z., 2016. Influence of mineralogy on the preservation of amino acids under simulated Mars conditions. Icarus 277, 342–353.
Edwards, H.G.M., Hutchinson, I., Ingley, R., 2012. The ExoMars Raman spectrometer and the identification of biogeological spectroscopic signatures using a flight–like prototype. Anal. Bioanal. Chem. 404, 1723–1731.
Ehlmann, B.L., Edwards, C.S., 2014. Mineralogy of the Martian surface. Annu. Rev. Earth Planet. Sci 42, 291–315.
Ehlmann, B.L., Mustard, J.F., Clark, R.N., Swayze, G.A., Murchie, S.L., 2011. Evidence for low-grade metamorphism, hydrothermal alteration, and diagenesis on Mars from phyllosilicate mineral assemblages. Clays Clay Miner 59, 359–377.
Ehlmann, B.L., Mustard, J.F., Murchie, S.L., 2010. Geologic setting of serpentine deposits on Mars. Geophys. Res. Lett. 37, 1–5.
Ehlmann, B.L., Mustard, J.F., Swayze, G.A., Clark, R.N., Bishop, J.L., Poulet, F., Des Marais, D.J., Roach, L.H., Milliken, R.E., Wray, J.J., Barnouin-Jha, O., Murchie, S.L., 2009. Identification of hydrated silicate minerals on Mars using MRO-CRISM: geologic context near Nili Fossae and implications for aqueous alteration. J. Geophys. Res. 114, E00D08.
Eigenbrode, J.L., Steele, A., Summons, R.E., Mcadam, A., Sutter, B., Franz, H.B., Freissinet, C., Millan, M., Glavin, D.P., Szopa, C., Conrad, P.G., Mahaffy, P.R., 2016. Preservation of organic matter on Mars by sulfur. AGU Fall Meet. P21D–08.
Emdadi, L., Tran, D.T., Zhang, J., Wu, W., Song, H., Gan, Q., Liu, D., 2017. Synthesis of titanosilicate pillared MFI zeolite as an efficient photocatalyst. RSC Adv 7, 3249–3256.
Emeline, A.V, Otroshchenko, V.A., Ryabchuk, V.K., Serpone, N., 2003. Abiogenesis and photostimulated heterogeneous reactions in the interstellar medium and on primitive earth: relevance to the genesis of life. J. Photochem. Photobiol. C Photochem. Rev. 3, 203–224.
Ertem, G., 2004. Montmorillonite, oligonucleotides, RNA and origin of life. Orig. life Evol. Biosph. 34, 549–570.
Ertem, G., Ertem, M.C., McKay, C.P., Hazen, R.M., 2016. Shielding biomolecules from effects of radiation by Mars analogue minerals and soils. Int. J. Astrobiol. 16 (3), 280–285.
Etiope, G., Ehlmann, B.L., Schoell, M., 2013. Low temperature production and exhalation of methane from serpentinized rocks on Earth: a potential analog for methane production on Mars. Icarus 224, 276–285.
Evans, N.L., Bennett, C.J., Ullrich, S., Kaiser, R.I., 2011. On the interaction of adenine with ionizing radiation: mechanistical studies and astrobiological implications. Astrophys. J. 730, 69.
Feil, S., Gluch, K., Matt-Leubner, S., Scheier, P., Limtrakul, J., Probst, M., Deutsch, H., Becker, K., Stamatovic, A., Märk, T.D., 2004. Partial cross sections for positive and negative ion formation following electron impact on uracil. J. Phys. B: At. Mol. Opt. Phys. 37, 3013–3020.
Flynn, G.J., 1996. The delivery of organic matter from asteroids and comets to the early surface of Mars. Earth, Moon Planets 72, 469–474.
Fornaro, T., Biczysko, M., Bloino, J., Barone, V., 2016. Reliable vibrational wavenumbers for C=O and N–H stretchings of isolated and hydrogen-bonded nucleic acid bases. Phys. Chem. Chem. Phys. 18 (12), 8479–8490.
Fornaro, T., Biczysko, M., Monti, S., Barone, V., 2014. Dispersion corrected DFT approaches for anharmonic vibrational frequency calculations: nucleobases and their dimers. Phys. Chem. Chem. Phys. 16 (21), 10112–10128.
Fornaro, T., Brucato, J.R., Branciamore, S., Pucci, A., 2013a. Adsorption of nucleic acid bases on magnesium oxide (MgO). Int. J. Astrobiol. 12, 78–86.
Fornaro, T., Brucato, J.R., Feuillie, C., Sverjensky, D.A., Hazen, R.M., Brunetto, R., D'Amore, M., Barone, V., 2018. Binding of nucleic acid components to the serpentinite-hosted hydrothermal mineral brucite. Astrobiology doi:10.1089/ast.2017.1784, Accepted.
Fornaro, T., Brucato, J.R., Pace, E., Cestelli-Guidi, M., Branciamore, S., Pucci, A., 2013b. Infrared spectral investigations of UV irradiated nucleobases adsorbed on mineral surfaces. Icarus 226, 1068–1085.
Fornaro, T., Brucato, J.R., Pucci, A., Branciamore, S., 2013c. Development of extraction protocols for life detection biosensor-based instruments. Planet. Space Sci. 86, 75–79.
Foustoukos, D.I., Stern, J.C., 2012. Oxidation pathways for formic acid under low temperature hydrothermal conditions: implications for the chemical and isotopic evolution of organics on Mars. Geochim. Cosmochim. Acta 76, 14–28.
Fraeman, A.A., Arvidson, R.E., Catalano, J.G., Grotzinger, J.P., Morris, R.V., Murchie, S.L., Stack, K.M., Humm, D.C., McGovern, J.A., Seelos, F.P., Seelos, K.D., Viviano, C.E., 2013. A hematite-bearing layer in Gale Crater, Mars: mapping and implications for past aqueous conditions. Geology 41, 1103–1106.
Franchi, M., Gallori, E., 2004. Origin, persistence and biological activity of genetic material in prebiotic habitats. Orig. life Evol. Biosph. 34, 133–141.
Frantseva, K., Mueller, M., ten Kate, I.L., Van der Tak, F.F.S., Greenstreet, S., 2018. Delivery of organics to Mars through asteroid and comet impacts. Icarus in press.
Franz, H.B., McAdam, A.C., Ming, D.W., Freissinet, C., Mahaffy, P.R., Eldridge, D.L., Fischer, W.W., Grotzinger, J.P., House, C.H., Hurowitz, J.A., McLennan, S.M., Schwenzer, S.P., Vaniman, D.T., Archer Jr, P.D., Atreya, S.K., Conrad, P.G., Dottin III, J.W., Eigenbrode, J.L., Farley, K.A., Glavin, D.P., Johnson, S.S., Knudson, C.A., Morris, R.V., Navarro-González, R., Pavlov, A.A., Plummer, R., Rampe, E.B., Stern, J.C., Steele, A., Summons, R.E., Sutter, B., 2017. Large sulfur isotope fractionations in Martian sediments at Gale crater. Nat. Geosci. 10, 658–662.
Freissinet, C., Glavin, D.P., Buch, A., Szopa, C., Summons, R.E., Eigenbrode, J.L., ..., Franz, H.B., 2016. First detection of non-chlorinated organic molecules indigenous to a Martian sample. 47th Lunar and Planetary Science Conference.
Freissinet, C., Glavin, D.P., Mahaffy, P.R., Miller, K.E., Eigenbrode, J.L., Summons, R.E., Brunner, A.E., Buch, A., Szopa, C., Archer, P.D., Franz, H.B., Atreya, S.K., Brinckerhoff, W.B., Cabane, M., Coll, P., Conrad, P.G., Marais, D.J.Des, Dworkin, J.P., Fairén, A.G., François, P., Grotzinger, J.P., Kashyap, S., Kate, I.L., Leshin, L.A., Malespin, C.A., Martin, M.G., Mcadam, A.C., Ming, D.W., Pavlov, A.A., Prats, B.D., Squyres, S.W., Steele, A., Stern, J.C., Sumner, D.Y., Sutter, B., Zorzano, M., 2015. Organic molecules in the sheepbed mudstone, Gale Crater, Mars. J. Geophys. Res. Planets 120, 495–514.
Gallori, E., Biondi, E., Franchi, M., 2004. Mineral surfaces as a cradle of primordial genetic material. In: Seckbach, J., Chela-Flores, J., Owen, T., Raulin, F. (Eds.), Life in the Universe, Cellular Origin and Life in Extreme Habitats and Astrobiology. Springer, Netherlands, pp. 145–148.
Garry, J.R.C., Ten Kate, I.L., Martins, Z., Nørnberg, P., Ehrenfreund, P., 2006. Analysis and survival of amino acids in Martian regolith analogs. Meteorit. Planet. Sci. 405, 391–405.
Georgiou, C.D., Sun, H.J., McKay, C.P., Grintzalis, K., Papapostolou, I., Zisimopoulos, D., Panagiotidis, K., Zhang, G., Koutsopoulou, E., Christidis, G.E., Margiolaki, I., 2015. Evidence for photochemical production of reactive oxygen species in desert soils. Nat. Commun. 6, 7100.
Gerakines, P.A., Hudson, R.L., 2013. Glycine's radiolytic destruction in Ices: first *in situ* laboratory measurements for Mars. Astrobiology 13, 647–655.
Glavin, D.P., Freissinet, C., Miller, K.E., Eigenbrode, J.L., Brunner, A.E., Buch, A., Sutter, B., Archer, P.D., Atreya, S.K., Brinckerhoff, W.B., Cabane, M., Coll, P., Conrad, P.G., Coscia, D., Dworkin, J.P., Franz, H.B., Grotzinger, J.P., Leshin, L.A., Martin, M.G., McKay, C., Ming, D.W., Navarro-González, R., Pavlov, A., Steele, A., Summons, R.E., Szopa, C., Teinturier, S., Mahaffy, P.R., 2013. Evidence for perchlorates and the origin of chlorinated hydrocarbons detected by SAM at the Rocknest aeolian deposit in Gale Crater. J. Geophys. Res. E Planets 118, 1955–1973.
Góbi, S., Bergantini, A., Kaiser, R.I., 2017. Degradation of adenine on the Martian surface in the presence of perchlorates and ionizing radiation: a reflectron time-of-flight mass spectrometric study. Astrophys. J. 838, 84.
Goetz, W., Brinckerhoff, W.B., Arevalo, r.J., Freissinet, C., Getty, S., Glavin, D.P., Siljeström, S., Buch, A., Stalport, F., Grubisic, A., Li, X., Pinnick, V., Danell, R., van Amerom, F.H.W., Goesmann, F., Steininger, H., Grand, N., Raulin, F., Szopa, C., Meierhenrich, U., Brucato, J.R., Team, the M.S., 2016. MOMA : the challenge to search for organics and biosignatures on Mars. Int. J. Astrobiol. 15, 239–250.
Gomes, R., Levison, H.F., Tsiganis, K., Morbidelli, A., 2005. Origin of the cataclysmic Late Heavy Bombardment period of the terrestrial planets. Nature 435, 466–469.
Grady, M.M., Verchovsky, A.B., Wright, I.P., 2004. Magmatic carbon in Martian meteorites: attempts to constrain the carbon cycle on Mars. Int. J. Astrobiol. 3, 117–124.
Greenwood, J.P., Blake, R.E., Coath, C.D., 2003. Ion microprobe measurements of $^{18}O/^{16}O$ ratios of phosphate minerals in the Martian meteorites ALH84001 and Los Angeles. Geochim. Cosmochim. Acta 67, 2289–2298.
Grim, R.J.A., Greenberg, J.M., 1987. Ions in grain mantles: the 4.62 μm absorption by OCN^- in W33A. Astrophys. J. 321, L91–L96.
Grotzinger, J.P., 2014. Habitability, taphonomy, and the search for organic carbon on Mars. Science 343, 386–387.
Hallis, L.J., Taylor, G.J., Nagashima, K., Huss, G.R., 2012. Magmatic water in the Martian meteorite Nakhla. Earth Planet. Sci. Lett. 359, 84–92.
Hammami, K., Feki, H.El, Marsan, O., Drouet, C., 2015. Adsorption of nucleotides on biomimetic apatite: the case of adenosine 5′ monophosphate (AMP). Appl. Surf. Sci. 353, 165–172.
Hashizume, H., van der Gaast, S., Theng, B.K.G., 2010. Adsorption of adenine, cytosine, uracil, ribose, and phosphate by Mg-exchanged montmorillonite. Clay Miner 45, 469–475.
Hassler, D.M., Zeitlin, C., Wimmer-schweingruber, R.F., Ehresmann, B., Rafkin, S., Eigenbrode, J.L., Brinza, D.E., Weigle, G., Böttcher, S., Böhm, E., Burmeister, S., Guo, J., Köhler, J., Martin, C., Reitz, G., Cucinotta, F.A., Kim, M., Grinspoon, D., Bullock, M.A., Posner, A., Gómez-elvira, J., Vasavada, A., Grotzinger, J.P., Team, M.S.L.S., 2014. Mars ' surface radiation environment measured with the Mars science laboratory's curiosity rover. Science 343 1244797–1–1244797–6.
Hausrath, E.M., Golden, D.C., Morris, R.V., Ming, D.W., 2008. Acid vapor weathering of apatite and implications for Mars. Lunar Planet. Sci. Conf. XXXIX.

Hausrath, E.M., Tschauner, O., 2013. Natural fumarolic alteration of fluorapatite, olivine, and basaltic glass, and implications for habitable environments on Mars. Astrobiology 13, 1049–1064.
Hermes-Lima, M., Tessis, A.C., Vieyra, A., 1990. Adsorption of 5′-adenosine monophosphate onto precipitated calcium phosphate: effects of inorganic polyphosphates and carbamyl phosphate. Orig. Life Evol. Biosph. 20 (1), 27–41.
Hoang-Minh, T., Le, T.L., Kasbohm, J., Gieré, R., 2010. UV-protection characteristics of some clays.. Appl. Clay Sci. 48, 349–357.
Hoffmann, M.R., Martin, S.T., Choi, W., Bahnemann, D.W., 1995. Environmental applications of semiconductor photocatalysis. Chem. Rev. 95, 69–96.
Holzmann, D., Holzinger, D., Hesser, G., Schmidt, T., Knör, G., 2009. Hydroxyapatite nanoparticles as novel low-refractive index additives for the long-term UV-photoprotection of transparent composite materials. J. Mater. Chem. 19, 8102–8106.
Hu, S., Lin, Y., Zhang, J., Hao, J., Feng, L., Xu, L., Yang, W., Yang, J., 2014. NanoSIMS analyses of apatite and melt inclusions in the GRV 020090 Martian meteorite: hydrogen isotope evidence for recent past underground hydrothermal activity on Mars. Geochim. Cosmochim. Acta 140, 321–333.
Hudson, R.L., Moore, M.H., Gerakines, P.A., 2001. The formation of cyanate ion (OCN-) in interstellar ice analogs. Astrophys. J. 550, 1140–1150.
Huestis, D.L., Bougher, S.W., Fox, J.L., Galand, M., Johnson, R.E., Moses, J.I., Pickering, J.C., 2008. Cross sections and reaction rates for comparative planetary aeronomy. Space Sci. Rev. 139, 63–105.
Hunten, D.M., 1979. Possible oxidant sources in the atmosphere and surface of Mars. J. Mol. Evol. 14, 71–78.
Jain, R., Awasthi, A.K., Tripathi, S.C., Bhatt, N.J., Khan, P.A., 2012. Influence of solar flare X-rays on the habitability on the Mars. Icarus 220, 889–895.
Jochims, H.-W., Schwell, M., Baumgärtel, H., Leach, S., 2005. Photoion mass spectrometry of adenine, thymine and uracil in the 6–22 eV photon energy range. Chem. Phys. 314, 263–282.
Klein, H.P., Horowitz, N.H., Levin, G.V, Oyama, V.I., Lederberg, J., Rich, A., Hubbard, J.S., Hobby, G.L., Straat, P.A., Berdahl, B.J., Carle, G.C., Brown, F.S., Johnson, R.D., 1976. The Viking biological investigation: preliminary results. Science 194, 99–105.
Klingelhöfer, G., Morris, R.V., Bernhardt, B., Schröder, C., Rodionov, D.S., de Souza, P.A., Yen, A., Gellert, R., Evlanov, E.N., Zubkov, B., Foh, J., Bonnes, U., Kankeleit, E., Gütlich, P., Ming, D.W., Renz, F., Wdowiak, T., Squyres, S.W., Arvidson, R.E., 2004. Jarosite and Hematite at Meridiani Planum from Opportunity's Mössbauer Spectrometer. Science 306, 1740–1745.
Kminek, G., Bada, J.L., 2006. The effect of ionizing radiation on the preservation of amino acids on Mars. Earth Planet. Sci. Lett. 245, 1–5.
Kounaves, S.P., Chaniotakis, N.A., Chevrier, V.F., Carrier, B.L., Folds, K.E., Hansen, V.M., McElhoney, K.M., O'Neil, G.D., Weber, A.W., 2014. Identification of the perchlorate parent salts at the Phoenix Mars landing site and possible implications. Icarus 232, 226–231.
Kundu, J., Neumann, O., Janesko, B.G., Zhang, D., Lal, S., Barhoumi, A., Scuseria, G.E., Halas, N.J., 2009. Adenine− and Adenosine Monophosphate (AMP)−gold binding interactions studied by surface-enhanced Raman and infrared spectroscopies. J. Phys. Chem. C 113, 14390–14397.
Lang, X.-F., Yin, P.-G., You, T.-T., Jiang, L., Guo, L., 2011. A DFT investigation of surface-enhanced Raman scattering of adenine and 2′-deoxyadenosine 5′-monophosphate on Ag_{20} nanoclusters. ChemPhysChem 12, 2468–2475.
Leroi, V., Bibring, J.-P., Berthe, M., 2009. Micromega/IR: Design and status of a near-infrared spectral microscope for *in situ* analysis of Mars samples. Planet. Space Sci. 57, 1068–1075.
Leulliot, N., Ghomi, M., Jobic, H., Bouloussa, O., Baumruk, V., Coulombeau, C., 1999. Ground state properties of the nucleic acid constituents studied by density functional calculations. 2. Comparison between calculated and experimental vibrational spectra of uridine and cytidine. J. Phys. Chem. B 103, 10934–10944.
Mahaffy, P.R., Webster, C.R., Atreya, S.K., Franz, H., Wong, M., Conrad, P.G., Harpold, D., Jones, J.J., Leshin, L.A., Manning, H., Owen, T., Pepin, R.O., Squyres, S., Trainer, M., 2013. Abundance and isotopic composition of gases in the Martian atmosphere from the curiosity rover. Science 341, 263–266.
McCollom, T.M., Donaldson, C., 2016. Generation of hydrogen and methane during experimental low-temperature reaction of ultramafic rocks with water. Astrobiology 16, 389–406.
McCubbin, F.M., Jones, R.H., 2015. Extraterrestrial apatite: planetary geochemistry to astrobiology. Elements 11, 183–188.
McCubbin, F.M., Shearer, C.K., Burger, P.V., Hauri, E.H., Wang, J., Elardo, S.M., Papike, J.J., 2014. Volatile abundances of coexisting merrillite and apatite in the martian meteorite Shergotty: implications for merrillite in hydrous magmas. Am. Mineral. 99, 1347–1354.
McKay, D.S., Gibson, E.K., Thomas-Keprta, K.L., Vali, H., Romanek, C.S., Clemett, S.J., Chillier, X.D., Maechling, C.R., Zare, R.N., 1996. Search for past life on Mars: possible relic biogenic activity in martian meteorite ALH84001. Science 273, 924–930.
Messenger, S., Keller, L.P., Lauretta, D.S., 2005. Supernova olivine from cometary dust. Science 309 (5735), 737–741.
Miller, K.E., Eigenbrode, J.L., Freissinet, C., Glavin, D.P., Kotrc, B., Francois, P., Summons, R.E., 2016. Potential precursor compounds for chlorohydrocarbons detected in Gale Crater, Mars, by the SAM instrument suite on the Curiosity Rover. J. Geophys. Res. Planets 121, 296–308.
Ming, D.W., Lauer, H.V, Archer, P.D., Sutter, B., Golden, D.C., Morris, R.V, Niles, P.B., Boynton, W.V, 2009. Combustion of organic molecules by the thermal decomposition of perchlorate salts: implications for organics at the Mars Phoenix Scout Landing site. In: 40th Lunar Planet. Sci. Conf. (Lunar Planet. Sci. XL), 40, p. 2241.
Möhlmann, D.T., 2004. Water in the upper martian surface at mid- and low-latitudes: presence, state, and consequences. Icarus 168, 318–323.
Möhlmann, D.T.F., 2008. The influence of van der Waals forces on the state of water in the shallow subsurface of Mars. Icarus 195, 131–139.
Morrison, S.M., Downs, R.T., Blake, D.F., Vaniman, D.T., Ming, W., Hazen, R.M., Treiman, A.H., Achilles, C.N., Yen, A.S., Morris, R.V, Rampe, E.B., Bristow, T.F., Chipera, S.J., Sarrazin, C., Gellert, R., Fendrich, K.V, Michael Morookian, J., Des Marais, D.J., Craig, P.I., 2018. Crystal chemistry of martian minerals from Bradbury Landing. Am. Mineral. in press.
Nassar, M.Y., Abdelrahman, E.A., 2017. Hydrothermal tuning of the morphology and crystallite size of zeolite nanostructures for simultaneous adsorption and photocatalytic degradation of methylene blue dye. J. Mol. Liq. 242, 364–374.
Negron-Mendoza, A., Ramos-Bernal, S., de Buen, I.G., 2010. A thermoluminescence study of bio-organic compounds adsorbed in a clay mineral. IEEE Trans. Nucl. Sci. 57, 1223–1227.
Nir, E., Kleinermanns, K., Grace, L., de Vries, M.S., 2001. On the photochemistry of purine nucleobases. J. Phys. Chem. A 105, 5106–5110.
Ody, A., Poulet, F., Bibring, J.P., Loizeau, D., Carter, J., Gondet, B., Langevin, Y., 2013. Global investigation of olivine on Mars: insights into crust and mantle compositions. J. Geophys. Res. E Planets 118, 234–262.
Ostovarpour, S., Blanch, E.W., 2012. Phosphorylation detection and characterization in ribonucleotides using Raman and Raman Optical Activity (ROA) spectroscopies. Appl. Spectrosc. 66, 289–293.
Oze, C., Sharma, M., 2005. Have olivine, will gas: Serpentinization and the abiogenic production of methane on Mars. Geophys. Res. Lett. 32, L10203.
Palomba, E., D'Amore, M., Esposito, F., Colangeli, L., Zinzi, A., 2004. Possible detection of apatite by infrared spectroscopy on Mars. Third Eur. Work. Exo-Astrobiol. 545, 255–256.
Patel, M.R., Bérces, A., Kolb, C., Lammer, H., Rettberg, P., Zarnecki, J.C., Selsis, F., 2003. Seasonal and diurnal variations in Martian surface ultraviolet irradiation: biological and chemical implications for the Martian regolith. Int. J. Astrobiol. 2, 21–34.
Patel, M.R., Zarnecki, J.C., Catling, D.C., 2002. Ultraviolet radiation on the surface of Mars and the Beagle 2 UV sensor. Planet. Space Sci. 50, 915–927.
Pedreira-Segade, U., Feuillie, C., Pelletier, M., Michot, L.J., Daniel, I., 2016. Adsorption of nucleotides onto ferromagnesian phyllosilicates: significance for the origin of life. Geochim. Cosmochim. Acta 176, 81–95.
Pilorget, C., Bibring, J.-P., Team, MicrOmega, 2012. The MicrOmega Instrument onboard ExoMars and future missions: an IR hyperspectral microscope to analyze samples at the grain scale and characterize early Mars processes. Third Conf. Early Mars 7006.
Poch, O., Jaber, M., Stalport, F., Nowak, S., Georgelin, T., Lambert, J.-F., Szopa, C., Coll, P., 2015. Effect of nontronite smectite clay on the chemical evolution of several organic molecules under simulated Martian surface ultraviolet radiation conditions. Astrobiology 15, 221–237.
Poch, O., Kaci, S., Stalport, F., Szopa, C., Coll, P., 2014. Laboratory insights into the chemical and kinetic evolution of several organic molecules under simulated Mars surface UV radiation conditions. Icarus 242, 50–63.
Poteet, C.A., Megeath, S.T., Watson, D.M., Calvet, N., Remming, I.S., McClure, M.K., Sargent, B.A., Fischer, W.J., Furlan, E., Allen, L.E., Bjorkman, J.E., Hartmann, L., Muzerolle, J., Tobin, J.J., Ali, B., 2011. A Spitzer infrared spectrograph detection of crystalline silicates in a protostellar envelope. Astrophys. J. 733, L32.
Powner, M.W., Gerland, B., Sutherland, J.D., 2009. Synthesis of activated pyrimidine ribonucleotides in prebiotically plausible conditions. Nature 459, 239–242.
Quinn, R.C., Martucci, H.F.H., Miller, S.R., Bryson, C.E., Grunthaner, F.J., Grunthaner, P.J., 2013. Perchlorate radiolysis on Mars and the Origin of Martian Soil Reactivity. Astrobiology 13, 515–520.
Ravanat, J.-L., Douki, T., Cadet, J., 2001. Direct and indirect effects of UV radiation on DNA and its components. J. Photochem. Photobiol. B Biol. 63, 88–102.
Riegel, G., Bolton, J.R., 1995. Photocatalytic efficiency variability in TiO2 particles. J. Phys. Chem. 99, 4215–4224.
Ryszka, M., Pandey, R., Rizk, C., Tabet, J., Barc, B., Dampc, M., Mason, N.J., Eden, S., 2016. Dissociative multi-photon ionization of isolated uracil and uracil-adenine complexes. Int. J. Mass Spectrom. 396, 48–54.
Sadjadi, S., Heravi, M.M., 2017. Current advances in the utility of functionalized SBA mesoporous silica for developing encapsulated nanocatalysts: state of the art. RSC Adv 7, 30815–30838.
Saladino, R., Botta, G., Delfino, M., Di Mauro, E., 2013. Meteorites as catalysts for prebiotic chemistry. Chem. Eur. J. 19, 16916–16922.
Saladino, R., Brucato, J.R., De Sio, A., Botta, G., Pace, E., Gambicorti, L., 2011. Photochemical synthesis of citric acid cycle intermediates based on titanium dioxide. Astrobiology 11, 815–824.
Saladino, R., Carota, E., Botta, G., Kapralov, M., Timoshenko, G.N., Rozanov, A.Y., Krasavin, E., Di Mauro, E., 2015. Meteorite-catalyzed syntheses of nucleosides and of other prebiotic compounds from formamide under proton irradiation. Proc. Natl. Acad. Sci. U. S. A. 112, E2746–E2755.
Scappini, F., Casadei, F., Zamboni, R., Franchi, M., Gallori, E., Monti, S., 2004. Protective effect of clay minerals on adsorbed nucleic acid against UV radiation: possible role in the origin of life. Int. J. Astrobiol. 3, 17–19.
Schoonen, M., Smirnov, A., Cohn, C., 2004. A perspective on the role of minerals in prebiotic synthesis. AMBIO: J. Hum. Environ. 33, 539–551.
Schuerger, A.C., Golden, D.C., Ming, D.W., 2012. Biotoxicity of Mars soils: 1. Dry deposition of analog soils on microbial colonies and survival under Martian conditions.. Planet. Space Sci. 72, 91–101.
Schutte, W.A., Greenberg, J.M., 1997. Further evidence for the OCN- assignment to the XCN band in astrophysical ice analogs. Astron. Astrophys. 317, L43–L46.

Schwartz, A.W., 2006. Phosphorus in prebiotic chemistry. Philos. Trans. R. Soc. Lond. B. Biol. Sci. 361, 1743–1749.
Senanayake, S.D., Idriss, H., 2006. Photocatalysis and the origin of life: Synthesis of nucleoside bases from formamide on TiO2 (001) single surfaces. Proc. Natl. Acad. Sci. U. S. A. 103, 1194–1198.
Shetlar, M.D., Basus, V.J., 2011. The photochemistry of uracil: a reinvestigation. Photochem. Photobiol. 87, 82–102.
Shkrob, I.A., Marin, T.M., Adhikary, A., Sevilla, M.D., 2011. Photooxidation of nucleic acids on metal oxides: physicochemical and astrobiological perspectives. J. Phys. Chem. C 115, 3393–3403.
Siljeström, S., Hode, T., Lausmaa, J., Sjövall, P., Toporski, J., Thiel, V., 2009. Detection of organic biomarkers in crude oils using ToF-SIMS. Org. Geochem. 40, 135–143.
Smith, M.D., Wolff, M.J., Lemmon, M.T., Spanovich, N., Banfield, D., Budney, C.J., Clancy, R.T., Ghosh, A., Landis, G.A., Smith, P., Whitney, B., Christensen, P.R., Squyres, S.W., 2004. First atmospheric science results from the Mars Exploration Rovers Mini-TES. Science 306, 1750–1753.
Souza-Egipsy, V., Ormö, J., Bowen, B.B., Chan, M.A., Komatsu, G., 2006. Ultrastructural study of iron oxide precipitates: implications for the search for biosignatures in the Meridiani Hematite Concretions, Mars. Astrobiology 6, 527–545.
Steele, A., McCubbin, F.M., Fries, M., Kater, L., Boctor, N.Z., Fogel, M.L., Conrad, P.G., Glamoclija, M., Spencer, M., Morrow, A.L., Hammond, M.R., Zare, R.N., Vicenzi, E.P., Siljeström, S., Bowden, R., Herd, C.D.K., Mysen, B.O., Shirey, S.B., Amundsen, H.E.F., Treiman, A.H., Bullock, E.S., Jull, A.J.T., 2012. A reduced organic carbon component in Martian basalts. Science 337, 212–215.
Steele, A., McCubbin, F.M., Fries, M.D., 2016. The provenance, formation, and implications of reduced carbon phases in Martian meteorites. Meteorit. Planet. Sci. 51, 2203–2225.
Sun, S., Chan, L.S., Li, Y.-L., 2014. Flower-like apatite recording microbial processes through deep geological time and its implication to the search for mineral records of life on Mars. Am. Mineral. 99, 2116–2125.
Szostak, J.W., 2009. Systems chemistry on early Earth. Nature 459, 171–172.
ten Kate, I.L., Garry, J.R.C., Peeters, Z., Foing, B., Ehrenfreund, P., 2006. The effects of Martian near surface conditions on the photochemistry of amino acids. Planet. Space Sci. 54, 296–302.
ten Kate, I.L., Garry, J.R.C., Peeters, Z., Quinn, R., Foing, B., Ehrenfreund, P., 2005. Amino acid photostability on the Martian surface. Meteorit. Planet. Sci. 40, 1185–1193.
ten Kate, I.L., Reuver, M., 2016. PALLAS: planetary analogues laboratory for light, atmosphere, and surface simulations. Netherlands J. Geosci. 95, 183–189.
Toporski, J., Steele, A., 2004. Characterization of purified biomarker compounds using time of flight-secondary ion mass spectrometry (ToF-SIMS).. Org. Geochem. 35, 793–811.
Tsuboi, M., 1970. Application of infrared spectroscopy to structure studies of nucleic acids. Appl. Spectrosc. Rev. 3, 45–90.
Varghese, A.J., 1971. Photochemistry of uracil and uridine. Biochemistry 10, 4283–4290.
Vesela, A., Wilhelm, J., 2002. the role of carbon dioxide in free radical reactions in organism. Physiol. Res. 51, 335–340.
Viviano-Beck, C.E., Seelos, F.P., Murchie, S.L., Kahn, E.G., Seelos, K.D., Taylor, H.W., ..., Morgan, M.F., 2014. Revised CRISM spectral parameters and summary products based on the currently detected mineral diversity on Mars. J. Geophys. Res. Planets 119, 1403–1431.
Weinbruch, S., Palme, H., Spettel, B., 2000. Refractory forsterite in primitive meteorites: condensates from the solar nebula? Meteorit. Planet. Sci. 35, 161–171.
Westall, F., 1999. The nature of fossil bacteria: a guide to the search for extraterrestrial life. J. Geophys. Res. Planets 104, 16437–16451.
Wright, I.P., Grady, M.M., Pillinger, C.T., 1992. Chassigny and the nakhlites: carbon-bearing components and their relationship to Martian environmental conditions. Geochim. Cosmochim. Acta 56, 817–826.
Yamauchi, O., Odani, A., Masuda, H., Sigel, H., 1996. Stacking interactions involving nucleotides and metal ion complexes. Met. Ions Biol. Syst. 32, 207.
Yen, A.S., Kim, S.S., Hecht, M.H., Frant, M.S., Murray, B., 2000. Evidence that the reactivity of the Martian soil is due to superoxide ions. Science 289, 1909–1912.
Zeynalov, E.B., Allen, N.S., 2006. Effect of micron and nano-grade titanium dioxides on the efficiency of hindered piperidine stabilizers in a model oxidative reaction. Polym. Degrad. Stab. 91, 931–939.
Zhao, L., Liu, Z., Zhang, X., Cui, T., Han, J., Guo, K., Wang, B., Li, Y., Hong, T., Liu, J., Liu, Z., 2014. Three-dimensional flower-like hybrid BiOI–zeolite composites with highly efficient adsorption and visible light photocatalytic activity. RSC Adv. 4, 45540–45547.